CRaTER: The Cosmic Ray Telescope for the Effects of Radiation Experiment on the Lunar Reconnaissance Orbiter Mission

CRaTER: The Cosmic Ray Telescope for the Effects of Radiation Experiment on the Lunar Reconnaissance Orbiter Mission

H. E. SPENCE, A.CASE, M. J. GOLIGHTLY, T. HEINE, B. A. LARSEN
Boston University

**J. B. BLAKE, P. CARANZA, W.R. CRAIN, J. GEORGE, M. LALIC,
A. LIN, M. D. LOOPER, J. E. MAZUR, D. SALVAGGIO**
The Aerospace Corporation

J. C. KASPER
Harvard-Smithsonian Center for Astrophysics

T. J. STUBBS
University of Maryland, Baltimore County and NASA/Goddard Space Flight Center

M. DOUCETTE, P. FORD, R.FOSTER, R. GOEKE, D. GORDON, B. KLATT, J. O'CONNOR, M. SMITH
Massachusetts Institute of Technology

T. ONSAGER
NOAA Spaceweather Prediction Center

C. ZEITLIN
Southwest Research Institute

L. TOWNSEND, Y. CHARARA
University of Tennessee, Knoxville

Abstract.

The Cosmic Ray Telescope for the Effects of Radiation (CRaTER) on the Lunar Reconnaissance Orbiter (LRO) characterizes the radiation environment to be experienced by humans during future lunar missions. CRaTER measures the effects of ionizing energy loss in matter due to penetrating solar energetic protons (SEP) and galactic cosmic rays (GCR), specifically in silicon solid-state detectors and after interactions with tissue-equivalent plastic (TEP), a synthetic analog of human tissue. The CRaTER investigation quantifies the linear energy transfer (LET) spectrum in these materials through direct measurements with the lunar space radiation environment, particularly the interactions of ions with energies above 10 MeV, which penetrate and are detected by CRaTER. Combined with models of radiation transport through materials, CRaTER LET measurements constrain models of the biological effects of ionizing radiation in the lunar environment as well as provide valuable information on radiation effects on electronic systems in deep space. In addition to these human exploration goals, CRaTER measurements also provide new insights on the spatial and temporal variability of the SEP and GCR populations and their interactions with the lunar surface. We present here an overview of the CRaTER science goals and investigation, including: an instrument description; observation strategies; instrument testing, characterization, and calibration; and data analysis, interpretation, and modeling plans.

Contents

1   Introduction

The Lunar Reconnaissance Orbiter (LRO) mission obtains exploration-enabling observations needed to facilitate returning humans safely to the Moon as part of NASA's longer-term Exploration Initiative. A NASA-established LRO Objectives/Requirements Definition Team (ORDT) identifies the following high-priority objective for this initial robotic mission in the Lunar Exploration Program (LEP): "Characterization of the global lunar radiation environment and its biological impacts and potential mitigation, as well as investigation of shielding capabilities and validation of other deep space radiation mitigation strategies involving materials." This critically-important LRO objective selected by the ORDT traces to earlier NASA planning documents, including the 1998 "Strategic Program Plan for Space Radiation Health Research" (Life Sciences Division, Office of Life and Microgravity Sciences and Applications, National Aeronautics and Space Administration).   Appendix H of that document summarizes the most critical questions concerning space radiation and its broad impact on all NASA activities. Strategic questions in the categories of space radiation environment, nuclear interactions, and human effects include:

- For a given mission, what are the fluxes of galactic cosmic rays (GCR) in interplanetary space as a function of particle energy, linear energy transfer (LET), and solar cycle?
- What are the doses related to heavy ions in deep space?
- How is a radiation field transformed as a function of depth in different materials?
- What are the optimal ways of calculating the transport of radiation through materials?
- What will the radiation environment be within the space vehicle, and what factors influence the flux, energy, and linear energy transfer spectrum of radiation?

The importance of this LRO objective and related outstanding questions is underscored in more recent NASA planning documents, such as the 2005 "Bioastronautics Roadmap: A Risk Reduction Strategy for Human Space Exploration". That document outlines several key goals including the development of new measurement approaches required for understanding the spectral properties of penetrating space radiation, and validating radiation shielding designs needed to define risk levels on exploratory-class missions and for risk mitigation. To date, these vitally important goals and questions remain open, in part because of limits in our ability to understand and simulate the evolution of radiation in space as it passes through human tissue. We are limited not only by scarce information about the cross sections for nuclear fragmentations at high energies but also by the lack of targeted observational data required to constrain radiation transport models.   While much is known and understood about radiation exposure in low earth orbit (c.f., Badhwar et al., 1996; Golightly et al., 1994), comparatively little is known at the Moon and in deep space.

The Cosmic Ray Telescope for the Effects of Radiation (CRaTER) instrument is designed *to characterize the global lunar radiation environment and its biological impacts*. CRaTER investigates the effects of galactic cosmic rays (GCR), solar energetic protons (SEP), and any secondary radiation produced by interactions between GCRs and SEPs at the lunar surface on tissue equivalent plastic (TEP) as a constraint for models of biological response to radiation in the lunar environment.   CRaTER

accomplishes this by producing linear energy transfer (LET) spectra over a wide dynamic range behind different areal densities of TEP and under different levels of solar activity and GCR flux. Functionally, CRaTER consists of a stack of circular silicon semiconductor detectors and cylindrical sections of TEP arranged so the ends of the stack have unobscured views of deep space and the lunar surface. Radiation passing through the stack, including ions and electrons, and to a lesser extent neutrons and gamma-rays, loses energy while passing through the silicon detectors. When ionizing radiation passes through a detector a signal is produced that is proportional to the total energy ΔE lost in the detector. Combined with the thickness Δx of the detector, an approximate LET is determined for the single particle as $LET = \Delta E / \Delta x$. Detectors are in pairs, with a thin detector connected to a low gain amplifier and a thick detector connected to a high gain amplifier. Together, the detector pairs and associated amplifiers make CRaTER sensitive to a broad range of LET from approximately $0.1 \, keV \, \mu m^{-1}$ to $2.2 \, MeV \, \mu m^{-1}$. By combining signals from different detectors to identify the path of individual particles, CRaTER can be used to understand how radiation loss evolves in human tissue and how dose rates change during periods of heightened solar activity and ultimately over the course of the solar cycle. Key unique capabilities of CRaTER are the inclusion of the TEP to make biologically relevant radiation measurements and a telemetry rate sufficient to capture high resolution LET values for up to 1,200 events per second. Whereas previous instruments were hampered by the need to reduce LET resolution or the number of events recorded owing to telemetry constraints, CRaTER will be able to produce spectra with high resolution in both LET and time.

This paper is structured as follows. Section 2 describes the CRaTER investigation, from science goals to measurement requirements and data products. We motivate the measurements needed and the resulting instrument design and discuss our anticipated results. Section 3 describes the instrument, from the telescope stack of TEP and silicon detectors that measure LET through the electrical design and the measurement process, our observing strategy, and science and housekeeping data products. Section 4 describes the instrument testing, characterization, and calibration. Section 5 describes the science operations center, as well as the data analysis, interpretation, and modeling. Finally, in Section 6, we summarize briefly several representative science studies made possible by CRaTER's design - a design intended initially for exploration-enabling measurements, but also capable of high quality science measurements of energetic particle phenomena at and near the Moon.

2 Investigation Description

2.1 Linear Energy Transfer and the LET Spectrometer

The measurement goal of CRaTER is to produce linear energy transfer (LET) spectra. LET ($\Delta E / \Delta x$) is the mean energy ΔE lost locally, per unit path length Δx, when a charged particle traverses material (LET is expressed in units of $MeV \, g^{-1} \, cm^2$, or, in a given system with known areal density, in $MeV \, \mu m^{-1}$). An LET spectrometer measures the amount of energy lost in a detector of some known thickness and material property as a high energy particle passes through it, usually without stopping. While LET spectrometers do not (necessarily) resolve mass, LET measurements do include all the

species, with the possible exception of neutrons, that are relevant to the energy deposited behind a known amount of spacecraft shielding. Relevant LET spectra are a missing link, currently derived largely by models, and require experimental measurements to provide critical ground truth – CRaTER will provide this essential quantity needed for model closure. Before proceeding further, we comment on the distinction between CRaTER LET measurements and the instantaneous energy loss rate, dE/dx. We recognize that instruments such as CRaTER typically cannot measure dE/dx directly because the detector has a finite thickness and the path length is not fully well-known for each particle detected. However, CRaTER is designed such that pathlength uncertainty is small (<10%). Additionally, by using sufficiently thin detectors, dE/dx is approximately constant within each detector. Consequently, as a large number of events are accumulated a spectrum of $\Delta E/\Delta x$ converges statistically to dE/dx (typically to within ~10%, the pathlength uncertainty).

As the particles comprising the solar and galactic cosmic ray environment penetrate shielding, whether the shielding is provided by spacecraft or habitat structure, or by an overlying atmosphere (such as on the Martian surface), or even by the body's own tissue that overlays a critical body organ, they lose energy due to the myriad of Coulomb interactions between the charged ions penetrating the material and the atomic electrons attached to the atoms and molecules of the target materials, and their nuclei. As these penetrating ions slow, their rates of energy loss to the target medium begin to increase. Hence their LET increases. On occasion, the nuclei of these penetrating ions undergo nuclear collisions with the nuclei of the target atoms. Occasionally the collisions are elastic, but more often than not, they are highly inelastic resulting in fragmentation (breakup) of the colliding nuclei. These lighter fragments, having lower charge and mass numbers than the parent nucleus, have reduced energy losses per distance traveled in the target medium, i.e. their LET decreases. Thus, the overall effects of the shield materials on the LET spectra are a complicated mixture of competing processes, which tend to significantly alter the LET distribution, making measured LET spectra dependent on the type, quantity, and geometric configuration of shielding that the incident particle spectrum has penetrated as well as on variations in the incident spectrum itself. In general, material shielding tends to reduce the overall fluence of high LET particles and increase the fluence of lower LET particles, for incident solar and GCR spectra.

A variety of LET measurements behind various thicknesses and types of material is of great importance to spacecraft engineers, radiation health specialists, and to modelers who estimate impacts of the penetrating radiation. LET is one of the most important quantitative inputs to models for predicting human health risks and radiation effects in electronic devices. By relaxing the demand to measure the entire parent cosmic ray spectrum to one where only that part of the energy spectrum deposited in a certain thickness of material is needed, the challenging requirements of measuring total incident cosmic ray particle energy is removed. This change in focus greatly simplifies the complexity, cost, and volume of the required instrument. And, in addition to these savings, an LET spectrometer essentially provides the key direct measurement needed to bridge the gap between well measured cosmic ray intensities that will be available from other spacecraft and specific energy deposition behind shielding materials, vital exploration-enabling knowledge needed for the safety of future astronauts working in the harsh space radiation environment.

2.2   Measurement Objectives

The first high level LRO measurement objective relevant to CRaTER is that *"The LRO shall characterize the deep space radiation environment at energies in excess of 10 MeV in lunar orbit, including neutron albedo"*. CRaTER is designed to measure the LET spectra of energetic particles across a range in charge and energy of biological relevance. One significant gap in knowledge of the deep space radiation environment is the uncertain LET spectra produced by the highest-energy, high-Z particles from both the Sun and the galaxy. While composition and variability of galactic cosmic rays above 10 MeV are fairly well defined, the spectra of the energetic component during intense solar energetic particle events is not well understood, demonstrates significant variability, and needs to be better specified. The current gap in understanding of this energetic component (> 10 MeV) is critically important. Thus, we aim to target > 10 MeV energies by virtue of their known damaging effects to man and machine and by virtue of their unpredictable time variability.   CRaTER will provide measurements of the deep space radiation environment above 10 MeV with a primary focus on charged particles. The LEND instrument on LRO is designed specifically to characterize the radiation effects of neutrons, the remaining aspect of the first LRO measurement objective (Mitrofanov et al, 2009).

The second LRO objective relevant to CRaTER is: "*The LRO shall measure the deposition of deep space radiation on human equivalent tissue while in the lunar orbit environment".* CRaTER will provide LET spectra behind different amounts and types of areal density, including tissue equivalent plastic. TEP is an inert solid substance that has radiation absorption characteristics similar to human tissue and has been used extensively in laboratory and space-based studies of radiation effects on humans. Understanding the evolution of the LET spectrum as it passes through human tissue is an important step in predicting, and possibly mitigating the effects of radiation on human bodies and spacecraft components.   The pathlength through CRaTER's TEP represents the characteristic depth of radiation penetration to blood forming organs.

2.3   Anticipated Results

The exploration goal of CRaTER is to provide the first deep space validation of radiation transport models. CRaTER will do so by producing LET spectra for comparison with simulation predictions. This validation is critical for transport models that are used to design shielding and estimate astronaut radiation risks.

Radiation transport models that take solar and galactic energetic particle spectra and produce predictions of evolving LET spectra within materials serve a critical role in risk reduction for the manned space program. For example, Kim et al. [1994] evaluated shield designs by calculating LET spectra using the 1977 solar minimum GCR spectrum as input into the "HZETRN" code. This simulation showed that LET curves decreased with increased shield thickness for high LET values but that for low LET values, the LET distributions increased, rather than decreased, with increasing shield thickness.   Predicted LET spectra are strong functions of both the materials used and uncertainties in nuclear processes. These

uncertainties are due to a lack of experimental data and to simplifications introduced into the models to speed up calculations. Simplified code is necessary to make the transport problem tractable and to permit exploration of a large number of possible configurations, but the simplifications also potentially limit model accuracy. The ability of these codes to accurately handle, for instance, spallation of heavy ions into lighter fragments and propagation through complex geometries and materials awaits experimental confirmation.

Once LET spectra data begin to be taken by CRaTER, the data can be used to aid in transport code validation for the lunar space radiation environment. Instruments on several NASA spacecraft such as ACE (Stone et al., 1998) and STEREO (Luhmann et al., 2007) as well as spacecraft from other agencies (e.g., NOAA–GOES) will be used to record the primary galactic and solar particle spectra contemporaneously. The populations measured at these high-altitude locations will serve as excellent proxies for the population of cosmic rays present at the lunar orbit at the same time (or at some easily calculated propagation time delay in the case of SEP events). Galactic cosmic rays are not considerably localized in space, so that measurements anywhere within several hundred Earth radii of the Moon will be sufficient. Transport models such as the HZETRN code developed at NASA Langley (J. W. Wilson et al., 1995) or the Monte Carlo code HETC-HEDS (Townsend et al., 2005), will then be used to predict the LET distributions seen by CRaTER. The comparison of our observed LET spectra with these predictions will allow us to provide closure between key measurements and models for understanding radiation effects.

To illustrate how CRaTER observations will be used to validate radiation transport models, Figure 1 shows a representative example of an LET spectrum. We created this spectrum using the Cosmic Ray Effects on MicroElectronics (CREME86) model with an input GCR spectrum based on the last solar minimum in 1996. The figure shows the LET spectrum in silicon expected behind 1mm of aluminum plotted in the same flux and LET units as planned for the CRaTER data products. Peaks in the spectrum are the result of major ion species (e.g., He) or ion groups (e.g., CNO). With such GCR rates, particularly for the heaviest ions that produce the largest and rarest response, LET spectra must be integrated over days, weeks, or months in order to resolve spectral features, intervals consistent with the one-year prime mapping duration of LRO. In later sections, we will show how CRaTER's design, in particular the ability to process and return unprecedented volumes of particle energy deposits, enables the construction of accurate LET spectra also over short time intervals, including during intense SEP events.

3   Instrument Description

Figure 2 illustrates the overall mechanical design of CRaTER, which physically consists of an electronics box and a telescope assembly. The instrument consists of a rectangular electronics box (approximately 24.1 cm long by 23.0 cm wide by 15.9 cm tall) with a slanted top cover. The electronics box bolts to the spacecraft through six feet along the base. The CRaTER telescope assembly attaches to the electronics box (see right portion of Figure 2). The telescope assembly and the electronics box are assembled separately and then integrated into the flight configuration as shown. The nadir, or lunar-

viewing, aperture of the telescope is delineated by the circular area on top of the telescope assembly in Figure 2. A normal to the circular aperture defines the telescope axis, which remains aligned along the nadir-zenith line during regular in-flight operations while LRO is in lunar polar orbit.

The electronics box houses a digital processing board (DPB) and an analog processing board (APB). The DPB interfaces with the spacecraft through the four connecters seen near the lower edge of the electronics box in Figure 2. These connectors serve to relay commands and telemetry, to provide power, and to provide a timing signal to CRaTER.

Figure 3 illustrates in cross-section the elements internal to the telescope assembly. The telescope assembly holds the telescope stack and the telescope electronics board (TEB). The TEB (green area) connects the telescope to the electronics box, delivers bias voltages to the detectors, and sends detector signals and calibration pulses through preamplifiers back to the APB. The preamplifiers are highly sensitive and so it is desirable to limit electrical interference near the detectors. Therefore the telescope assembly is electrically isolated from the electronics box, and grounded on the same path as the signals from the preamplifiers to the APB. The telescope stack consists of aluminum caps on the nadir (top end cap in Figure 3) and zenith (bottom end cap) sides to shield the telescope detectors from low energy particles, followed by three pairs of thin and thick silicon detector pairs surrounding two sections of A-150 Tissue Equivalent Plastic (TEP) of different length (dark grey areas).

Figure 4 shows a functional block diagram of the entire CRaTER instrument, from detectors to the spacecraft bus; data flows from left to right in this block diagram. It shows the most critical components necessary for reliable functioning of the instrument. As described above, the telescope assembly houses the telescope stack of detectors and TEP, and the telescope board. The electronics box assembly houses the APB and the DPB. The APB shapes the pulses from each of the detector preamplifiers, further amplifies the signals, and generates calibration pulses for testing the response of each signal path. The DPB identifies and processes particle events and generates scientific measurements, controls power distribution within the instrument, records housekeeping data, and receives commands and sends telemetry to the spacecraft.

Table 1 summarizes the main properties of the CRaTER instrument, including physical resources, key design values, and measurement performance metrics. These quantities of the as-delivered flight model represent the optimal values resulting from science and engineering trade studies completed throughout the instrument development. The remainder of Section 3 describes details of the design which drive and determine the high-level values shown in Table 1.

3.1 Telescope Design

3.1.1 Overview

In this section, we summarize the physical construction of CRaTER, with a focus on the sensing portion of the instrument, or the telescope assembly. As described in the instrument overview, CRaTER consists of two physical parts, the telescope assembly and the electronics box. The telescope is

mechanically mounted to the electronics box, but the two structures are electrically isolated from one another. The entire telescope assembly is instead grounded to the analog signal ground. This is done to reduce noise on the spacecraft chassis ground reaching the sensitive detectors and their preamplifiers.

As illustrated and identified in Figure 5, the CRaTER telescope stack consists of three pairs of thin and thick detectors surrounding two pieces of TEP. From the zenith side of the stack the components are the zenith shield (S1), the first pair of thin (D1) and thick (D2) detectors, the first TEP absorber (A1), the second pair of thin (D3) and thick (D4) detectors, the second TEP absorber (A2), the third pair of thin (D5) and thick (D6) detectors, and the final nadir shield (S2). We shall use these shorthand designations henceforth. With this configuration, paired thin and thick silicon detectors thereby measure the LET spectrum at three depths through the telescope stack. Section 3.1.2 reviews the detectors selected for CRaTER and discusses the need for the pairs of thin and thick detectors to cover the full range of LET possible in silicon. The three pairs of detectors cover the range in LET expected by SEP and GCR ions in silicon and after evolving through the telescope assembly, including passage through the dominant component, the TEP. Section 3.1.3 describes the A-150 Tissue Equivalent Plastic used as the human tissue analog and primary absorber. Section 3.1.4 describes the optimization of the location of components in the telescope stack.

Key factors guiding our design of the telescope stack were the total pathlength through TEP desired, the sizes of the different pieces of TEP, and the geometric factor and resulting sensitivity of the entire telescope. By requiring that the minimum energy of protons that can just exit the TEP be ~100 MeV and that the TEP rather than the silicon in the detectors dominates the areal density of the telescope stack, we identified a goal pathlength through the total amount of TEP in the telescope of ~60 mm. Our design divides the total TEP pathlength into two components of different length, 1/3 and 2/3 the total length of the TEP. If the total TEP is 71 mm in length, then the TEP section closest to deep space will have a length of approximately 54 mm and the second section of TEP will have a length of approximately 27 mm. A variety of LET measurements behind various thicknesses and types of material is of great importance to spacecraft engineers, radiation health specialists, and to modelers who estimate impacts of the penetrating radiation. Simulations suggested that splitting the TEP into two asymmetric components that are 1/3 and 2/3 the total length provides a useful combination of lengths, also similar to typical thicknesses through human tissue to depths of blood forming organs.

Statistically significant LET spectra should be accumulated over short enough time intervals to resolve dynamical features in the galactic cosmic ray (GCR) and solar energetic particle (SEP) flux. During quiescent intervals, the counting rate will be dominated by the slowly varying GCR light ions. With typical GCR fluxes expected for solar minimum conditions (Webber and Lezniak, 1974), a minimum geometric factor of 0.57 cm^2sr (shown later to be the as-designed value) will yield LET rates of ~ 0.3 events/second from protons with incident energy sufficient to pass through the entire telescope. In one hour, a statistically significant sampling of ~1000 events would permit construction of longer-term average spectra; this one-hour interval is still short compared to typical GCR modulation timescales.

The geometric factor of a cylindrical telescope of this type is a function of both the distance between the detectors and the diameter of the detectors. We conducted a trade study to select the

11

diameter of the CRaTER detectors. Our study focused on the benefit of a larger diameter detector in the form of larger collecting areas and geometric factors, versus the risk of unacceptably high single particle fluxes during major solar energetic particle (SEP) events. While both protons and heavy ions are enhanced during SEP events, the flux of hydrogen is many orders of magnitude larger and their detection dominates the counting rates. The hydrogen therefore was the focus of this trade study.

The first thick detector in the zenith (deep space) direction, D2, is designed to detect protons and is therefore most susceptible to enhanced fluxes during SEP events. The other thick detectors lie behind shielding in the form of the TEP and telescope mass and ultimately the Moon below, and are therefore expected to have lower rates. The concern is not that the D2 detector could be damaged by the high flux, but rather that it could experience electronic pulse pileup, in which multiple protons pass through the detector within a detection interval and corrupt the signal. The predicted worst-case singles count rate for D2 is shown in Figure 6, estimated from the >10 MeV proton channel on the GOES spacecraft during the 225 most extreme SEP events over the last 33 years.. Peak, instantaneous (5 minute average) proton rates are combined with the D2 single-detector geometric factor (~30 cm^2-sr) for this analysis We find that CRaTER's normal operation mode is sufficient to robustly measure all particles for ~90% of the peak rates encountered during extreme SEP events. To recover the remaining 10%, CRaTER is deliberately designed to reconfigure in response to such especially high rates. If the D2 signal saturates and thereby would otherwise overwhelm event processing with low energy protons, CRaTER has additional features to avoid any decrease in the utility of the measurements returned to the ground; this rate event mode switching is described fully at the end of Section 3.3.6.

3.1.2 Detectors

CRaTER uses silicon semiconductor detectors to characterize the rate of energy loss of charged particles passing through the telescope. In this section we motivate our choice of detector thicknesses and the LET ranges the detectors are used to measure. We begin by reviewing the operating principles of semiconductor detectors. Figure 7 depicts a simplified detector cross-section illustrating the key components of the CRaTER detectors. At energies of interest to CRaTER, silicon semiconductor detectors are useful for characterizing the energy loss of ionizing radiation as it passes through or stops in it. In the CRaTER detectors, silicon is doped to make it a semiconductor, with electron-hole pairs in valance levels with energy levels much smaller than the first ionizing potential of an atom, making the detector much more sensitive than a proportional counter. The silicon is composed of both an N-type and a P-type substrate, making it a large diode that can be biased at a relatively high voltage with little leakage current.

When an energetic charged particle passes through the silicon, it liberates electron-hole pairs, which rapidly drift to either end of the detector in the electric field established by the bias voltage. The resulting signal from the drifting electron-hole pairs is linearly proportional to the total energy deposited. An analog circuit is then used to amplify these signals when they occur, and to stably and

accurately determine the height of each pulse in multiple detectors. Both detector types are ion-implanted, totally-depleted structures formed from an N-type substrate. The Phosphorous-implanted N-type substrate is the ohmic side of the detector and the Boron-implanted P-side is the junction. These impurities generally require lower implantation energies and thus result in low implant depths of about 0.3μm. Both detector areas are circular, have thin junction and ohmic windows, and have relatively fast timing capability, meaning that the electron hole pairs rapidly diffuse to the surfaces and provide a sharp signal to the electronics. Although fast timing is not critical for CRaTER, it is desired to have the metallization made in such a fashion as to reduce surface resistivity. There is a guard ring (indicated by the region labeled Guard) around the active junction to improve edge uniformity and a neighboring field plate ring to aid discharge of oxide stray charge. Each thin and thick detector mounts to its own small passive printed circuit board and connects to the telescope electronics board by a flexible cable.

Thin and thick detector pairs are used to span the entire range of LET and to provide a system that is less sensitive to low energy protons in the event of intense SEPs associated with solar flares and coronal mass ejections. The thickness of the thin detectors is approximately 150 microns while the thick detectors are approximately 1000 microns. The need for pairs of detectors arises from the large range in LET that ions can produce in silicon through ionizing radiation and from the different amplitudes of energy loss expected from light and heavy cosmic ray ions. In order to understand the range of LET expected in the detectors, we review the common modes of energy loss by a moderately relativistic particle.

A moderately relativistic proton or heavier charged ion passing through a medium such as human tissue, TEP, or the silicon detectors will lose energy through electromagnetic interactions with electrons in the medium and through weak and strong interactions with nucleons. Generally the nuclear interactions are less common, but they become more important for the heavier ions above $20\ MeV/nuc$ and are a major source of uncertainty in predicting LET. Nuclear interactions are also a mode whereby neutrons can produce a signal in the CRaTER detectors, although this process is also uncommon. For the purposes of optimizing CRaTER, we focus on electromagnetic energy loss. The average rate of energy loss, or stopping power, of energetic but not ultra-relativistic charged particles other than electrons is given by the Bethe-Bloch equation. The energy loss dE/dx of a particle with charge z, energy E, and speed $\beta = v/c$ passing through a medium with atomic number Z and atomic mass A is given by,

$$-\frac{dE}{dx} = Kz^2 \frac{Z}{A} \frac{1}{\beta^2} \left[\frac{1}{2} \ln \left(\frac{2m_e c^2 \beta^2 \gamma^2 T_{max}}{I^2} \right) - \beta^2 \right] \qquad MeV\ g^{-1} cm^2$$

where $K = 0.307075\ MeV\ g^{-1} cm^2$, m_e is the electron mass, c is the speed of light, $\gamma^2 = 1/(1 - \beta^2)$, T_{max} is the maximum energy that the ionizing particle can impart in a single collision, and I is the minimum energy required to excite the medium (Yao et al., 2006). There is a strong dependence of the stopping power on the charge of the incident particle, and a weaker dependence on the mass of the particle through T_{max}. Corrections exist at both high energies, where polarization and shielding effects become more difficult to treat, and at low energies where assumptions about the adiabaticity of the collisions become invalid. Additionally, an ion will experience multiple Coulomb scatterings, leading to a

trajectory that deviates from a straight line. This leads to a statistical distribution in the path length that a given species of particles will traverse in passing through or stopping in the detector, even with identical initial energies. This results in the phenomenon of "straggling", which will manifest itself as a finite width in the range of energy deposited by a single type and energy of particle, no matter how fine the energy resolution of the detector or how low the noise level. This "noise" in the signal due to straggling places a lower limit on the energy resolution needed to distinguish events. Three implications of the Bethe-Bloch equation are that the energy deposited in the detectors increases with the square of the charge of the ionizing particle (so iron will deposit much more energy than hydrogen), that the peak of the energy deposition occurs as the particle is just stopping in the detector, and that the minimum-ionizing radiation rate occurs at ~2 Gev/nuc. Consequently, we set the minimum measurable LET to that of minimum-ionizing protons in silicon. The maximum LET is set by the energy that an iron nucleus will deposit when it just stops in a thin detector. Figure 8 shows projected range and LET of iron in silicon using SRIM (Ziegler et al., 1984). SRIM (The Stopping and Range of Ions in Matter) is a group of programs which calculates the stopping and range of ions (10 eV - 2 GeV/nuc) into matter using a full quantum mechanical treatment of ion-atom collisions.

The CRaTER telescope uses pairs of thin (~150 micron) and thick (~1000 micron) detectors. As discussed in the electronics section, the thin detectors are connected to a low gain amplifier, while the thick detectors are operated with a high gain. This design makes the thick detectors sensitive to particles with very low LET, while a very high LET is required to produce a measurable signal in the thin detectors. This use of high and low gain thin and thick detectors is motivated by the range of LET we need to measure at each point in the telescope stack and in the infeasibility of doing that broad an LET range with a single detector. Within the limits of the noise level of the detectors, it is desirable to detect high energy particles with the minimum ionizing deposition rate, so each point in the telescope where the LET spectrum is to be observed, the minimum LET measured shall be no greater than 0.25 keV/micron in the silicon. Practical considerations effectively constrain the high end of the LET energy range. Slow moving, high-Z ions that give up much of their energy upon interaction will by definition yield large LET events. Therefore, the instrument should be able to measure such high-Z particles. On the other hand, the probability of a high energy heavy ion just stopping in a detector and depositing the maximum signal is small. Models and observations of heavy ions with prototype instruments show that these particles will produce signals commensurate with a deposition of 2 MeV/micron, so at each point in the telescope where the LET spectrum is to be observed, the maximum LET measured shall be no less than 2 MeV/ micron in the silicon.

3.1.3 Tissue Equivalent Plastic and Composition of CRaTER materials

As discussed in the previous section, the evolution of LET spectra is determined both by the composition of the incident high energy radiation and by the composition of the material being encountered. This is especially significant when considering biological effects. For example, one study has shown that as radiation travels through organic matter, the contribution to biological change

(gauged by the neoplastic transformation of C3H101T/2 mouse cells, a well studied cell line) from light ions increases, while the importance of heavy ions (such as iron) decreases (Kim et al., 1994). At equivalent depths of approximately 5 g/cm^2, hydrogen and helium are the dominant contributors to the measured biological change. Since the LET spectrum is such a sensitive function of the absorbing medium, the bulk of the material within CRaTER must be similar to human tissue in order to produce results related to biological effects. Furthermore, the volume of TEP employed must be sufficient to cover the range in depths where the dominant species is expected to change from heavy to light ions.

The muscle equivalent tissue equivalent plastic (TEP) A-150 is the most popular material used today in the construction of instruments that measure the evolution of ionizing radiation in the presence of materials similar to human tissue. A150 is an Exradin proprietary plastic blend designed to be tissue equivalent. It is also known as Shonka tissue equivalent plastic after its original creator, Francis Shonka. By material, A-150 TEP is a combination of Polyethylene, Polyamide, Carbon black, and Calcium fluoride. TEP has the appearance of a black crayon but is very stiff and is easily machined. The TEP is slightly hydroscopic, and will absorb up to ~3% water by weight in a 50% humidity environment. Our tests showed that other than the water, little material outgassed from TEP samples after they were baked out in a vacuum. The composition and thicknesses of the TEP used in CRaTER is given in Table 2; the detailed TEP composition and dimensions are important as inputs to radiation transport code models.

The two pieces of TEP used in the telescope stack have a 2:1 length ratio, with the longer component on the deep space side of the telescope. The pieces are right cylinders and are held firmly in place at each end. The three thick-thin detector pairs sandwich the two pieces of TEP. The different lengths produce an asymmetric geometry. This configuration serves several purposes. The initial LET spectrum is measured at D1/D2 after first passing through the thin aluminum zenith cap. (Since the aluminum end caps are part of the material traversed by detected particles, and because the material properties of this matter is important also for a robust model comparison, we include Table 3 which shows the detailed composition and thicknesses of the end cap aluminum. In addition, a thin single layer of thermal blanket material covers each end cap on the exterior of the telescope.) After passing through D2 the LET spectrum is representative of the corresponding spectrum that would be present just on the inside of a manned space vehicle. The particles then traverse the longer piece of TEP whose length of several inches is similar to the depth to blood-forming organs in a human body. D3/D4 measure and quantify the evolution of the LET spectrum after passing through this first length of TEP. Those particles with enough energy then traverse the second, shorter TEP segment simulating a longer pathlength to a blood-forming organ. D5/D6 measures the fully evolved LET spectrum resulting from passage of particles through the entire length of the telescope.

3.1.4   Fields of View and Geometric Factors

Motivated by the need for sensor simplicity and in keeping with the primary measurement requirement, CRaTER does not determine the vector trajectory of individual particles (through position sensing strips, for example). Additionally, no means are employed to identify particles that pass through the side of the instrument and are detected (using a scintillator shroud surrounding the entire telescope stack coupled to a photo-multiplier tube, for example). Such techniques are often used to constrain the pathlength traversed by particles in a cosmic ray telescope and to reject events consisting of multiple particles or which scatter out of the instrument volume. Since we are interested in studying the spectrum of all particles within the telescope, including those that scatter at large angles, and because the techniques described above introduce a great deal of complexity, telemetry, and mass, we instead define the fields of view of the instrument (and hence statistically well-constrained path lengths) through n-fold detector coincidences.

The CRaTER measurement requirements place constraints on the field of view of the instrument only indirectly, through restrictions on the uncertainty in the pathlength traversed through the TEP and the detectors, and through lower limits on geometric factors, for example. While large fields of view are not a requirement, they are desirable in that they increase the geometric factor and therefore the statistical accuracy of the LET spectral measurements, particularly of the low intensity GCR population. In addition, since it is possible that SEPs and GCRs reflecting off the lunar surface – especially at small grazing angles of incidence – could provide significant diagnostics of the composition of the Moon and of secondary radiation from the surface, it is desirable that the nadir end of the telescope have as large a field of view as possible (owing to the presumed lower flux of cosmic ray albedo). This is another driver for having the shorter piece of TEP on the nadir end of the telescope as the D3/D4 and D5/D6 coincidences define a relatively larger opening angle than do D1/D2 and D3/D4.

The optimization of the CRaTER fields of view is discussed in the following section. Here we note the fields of regard that the spacecraft is able to support for the instrument. It is essential that the fields of view of CRaTER are not obstructed by components of the spacecraft, as CRaTER will not be able to distinguish between the primary spectrum of GCRs and SEPs and the secondary spectrum produced by interactions with spacecraft components.

The final spacing between the components of the telescope stack was determined by conducting a trade study that identified the configuration which optimized the parameters captured in the design requirements. The instrument requirements that are affected by the telescope stack are the following: 'the minimum pathlength through the TEP should be >60 mm' and 'the two pieces of TEP should be different lengths (herein chosen to be 1/3 and 2/3 of the total length)'. In order to have sufficient counting rates of the most energetic particles during normal times CRaTER should have a minimum, full telescope geometric factor of ~ 0.1 cm^{2}sr. In order to yield a sufficiently small uncertainty on the inferred LET, a geometry which produces <10% variation in path length between D1 and D6 is required. We constrained both the zenith and nadir field of view to be within their fields-of-regard (35 and 85 degrees, respectively). Owing to the proximity of CRaTER to the spacecraft, some fields-of-view defined by detector coincidences intercept part of the spacecraft.   However, the required fields-of-regard assure unobstructed views of deep space for particles producing six-fold detector coincidences

and for those producing a D4-D6 coincidence from the nadir direction. Furthermore, these two important view geometries are also unobstructed by the instrument itself.

We found that the telescope stack optimization could be expressed by varying two free parameters, which we called L1 and L2. L1 is the length between the top of detector D2 and the top of detector D4, and L2 is the length between the top of detector D2 and the top of detector D6. We considered other heights less important. For example, the spacing between the thin and thick detectors in each pair is set by the natural value of the printed circuit boards the detectors are mounted on. We found that placing the zenith and nadir shields further away from the closest detector pair only increased the necessary diameter of the shield needed to provide a uniform thickness over the field of view. Therefore the shields are simply best put close to the adjacent detectors, as limited solely by sensible design practices. Since the TEP sections have a sufficiently larger diameter than the detectors, it did not make a practical difference where the TEP was mounted relative to the detector pairs. Thus, L1 and L2 summarize the two unique parameters varied in the trade study.

From this trade study the optimal values set a D1-D6 geometric factor of 0.57 cm^2sr with a zenith or nadir field of view of 31.4^o , well within the zenith and nadir fields of regard. In addition, the D4-D6 coincidence provides a geometric factor of 2.564 cm^2sr and a field of view of 65.9^o, again within the nadir field of regard. In the nominal LRO orbit (polar inclination, 30-50 km lunar altitude) this nadir field of view is completely filled by the lunar surface, thus maximizing the probability of detecting albedo particles.

Table 4 contains the critical linear dimensions of telescope elements along the resulting optical path. The detector diameters are each 35 mm and all other components have diameters slightly greater than 35 mm. Table 5 contains the resultant fields of view for key representative detector coincidences along with their geometric factors. The final column shows the threshold proton energy needed to create the coincidence from the indicated direction of incidence ("z" for zenith and "n" for nadir). Finally, Figure 9 shows the minimum energy required of ions (hydrogen to iron, using each ion's most common isotope) normally-incident from zenith to reach D2, D4, and D6.

The geometric factors presented in Table 5 are based purely on geometry and coincidence requirements. For particles passing through the sides of the instrument, detectors will have a complex and energy-dependent geometric factor. It is important to understand and limit the sensitivity of the detectors to such side penetrators, in order to limit false coincidences and to maximize performance during high flux intervals. To this end, reserve mass was placed in a thick ring around each detector pair (see Figure 2). We used GEANT4 to show that this extra shielding mass, along with the instrument housing, provides effective shielding of side penetrating protons up to typically ~50 MeV.

3.2 Electrical Design

3.2.1 Overview

In this section we cover the flow of electrical signals from the detectors through the telescope board to the analog processing board and finally the digital processing board. A key electrical aspect of the overall design of CRaTER is that the telescope housing is connected to the analog ground inside the telescope assembly, and nowhere else. The telescope housing is electrically isolated from the electronics box in order to prevent noise coupling from the spacecraft into the detector front-end. The electronics box housing is connected to the digital ground inside the electronics box.

A high-resolution measurement of the energy deposited is required to characterize the LET spectrum and to distinguish between the effects of the primary radiation and secondaries produced through interactions. The pulse height analysis of the energy deposited in each detector shall have an energy resolution better than 1/200 the maximum energy measured by that detector.

3.2.2 Telescope Board

The purpose of the telescope board is to bias each of the detectors, and to provide for an initial pre-amplification of the signals in close proximity to the detectors in order to reduce noise as the small initial signal is transported. Figure 10 is a block diagram of the components of the telescope board for a single detector.

3.2.3 Analog Processing Board

The Analog Processing Board (APB) provides a linear transfer function of output signal amplitude to detector energy deposit for three thin detectors and three thick detectors. A functional block diagram of a single amplifier string is shown in Figure 11. The signal from the preamplifier is passed through a system to remove constant offsets and give the signal a symmetric Gaussian profile. The thin and thick detector signals are Gaussian shaped pulses with a peaking time of ~$1\mu s$. This pulse shaping time was optimized by a consideration of the noise level of the thick detectors at 20C as a function of the shaping time. The design architecture for the APB is drawn from significant flight heritage such as in the Imaging Proton Spectrometer instrument on the NASA Polar spacecraft (Blake et al., 1995).

3.2.4 Digital Processing Board

The purpose of the Digital Processing Board (DPB) is to identify events that are valid for pulse height analysis, digitize the pulse-heights of the APB output signals, provide control of APB test pulser, supply power and detector bias, and provide the command and telemetry interface to the spacecraft. Figure 12 is a block diagram of the functions of the field-programmable gate array (FPGA) and the DPB.

Test Pulse Generator

An internal pulse generator is used during ground test phases and in orbit to monitor the stability of the pulse forming network with time and to perform instrument aliveness tests. The test pulse generator injects a known charge into the front of each preamplifier with two gain settings, an 8-

bit resolution amplitude, and low (8 Hz) and high (2 kHz) frequency rates. A connection is available for each detector for the injection of externally generated pulses. This external option was used on the ground to distinguish between noise and variation in the APB and in the test pulse generator and is not available in flight.

Low Level Discriminator

Two Low Level Discriminator (LLD) threshold voltages are generated by converting Pulse Width Modulated FPGA outputs to DC voltages. The discriminator amplitude, set via the 8-bit command interface registers, ranges from -0.047 to 0.141 V-DC. The thin detector discriminator setting drives the D1, D3 and D5 comparators; the thick detector discriminator setting drives the D2, D4 and D6 comparators. The instrument does not perform a pulse height analysis for an event unless the energy deposited in at least one detector produces a signal stronger than its corresponding LLD threshold.

3.2.5   Power
The DPB monitors and enables low voltage DC-DC converters that changes the 28VDC provided by the spacecraft into +/- 5V for use by the analog electronics, and a separate +5V for use by the digital electronics and bias supplies. The bias voltages were designed to be about 30 volts higher than the full depletion voltage of the detectors over a large range of leakage currents. The thin detector bias is approximately +75V and the thick detector bias is approximately +225V.

3.3   CRaTER Measurements

3.3.1   Overview
If a particle deposits enough energy in a detector, then a primary science measurement will be triggered. The measurement is of the energy deposited separately in each of the six detectors. It should be noted that regardless of which detector(s) cross their respective LLD thresholds, all six detectors are analyzed and reported in the data.

3.3.2   Measurement Sequence
The primary science measurements consist of the amplitudes of pulses detected from each of the detectors. The six signals from the pulse-forming and amplification networks on the APB are sent to the digital board, where the signals from the thin and thick detectors are separately compared to a low level discriminator (LLD) reference voltage. If any of the six signals crosses the corresponding LLD threshold, then a pulse height analysis (PHA) of all six signals is triggered.

After the PHA is complete, the list of triggered detectors is compared with a programmable mask that encodes the sets of detector coincidences that correspond to events of interest for subsequent analysis on the ground. If an event falls within the mask set, it is added to a telemetry buffer within the FPGA (a "good" event), otherwise it is discarded (a "reject" event). With the exception of extreme high rate events, CRaTER shall operate with a coincidence mask that accepts all possible detector coincidences (i.e., virtually all particle detections are telemetered to the ground).

Figure 13 provides a schematic illustration of the pulse height analysis. At some time T<0μs a current pulse produced by either migrating electron-hole pairs in the detector or a test pulse from the digital board passes through the preamplifier in the telescope board and arrives at the analog board. At T=0μs the signal from the preamplifier crosses the low level discriminator (LLD) and triggers the PHA. At T=2μs the peak detect is set to hold and the analog-to-digital converter (ADC) is commanded to power up. At T=4μs the ADC is powered up and does a sample and hold in the following two clock cycles. The ADC then performs a serial conversion over the next 12 clock cycles, clocking the results out to the digital board. About 1/3 of the way through the ADC the peak detector is reset. The ADC and the measurement process is complete at T=12μs, defining the fixed measurement dead time.

3.3.3   Science Data Products

Primary Science Data Products

The event data for a single event in the primary science packet consists of a 9-byte block containing the six 12-bit numbers corresponding to the pulse height analysis of the six detectors. The FPGA contains two buffers. While primary science data are being written to one buffer during a given one second interval, the FPGA reads out the data stored in the previous second from the other buffer.

Secondary Science Data Products

Secondary science telemetry packets are read during every 1-second data interval in which primary science data are being collected. These secondary science values set the time resolution that the state of the instrument (calibration commands, bias supply status, and disabling of detector processing) can be tracked on the ground. Parameters included in the secondary science data stream include: whether or not the calibration system is enabled, the calibration system rate, whether or not the thin and thick detectors are biased, whether or not each detector processing is enabled, and information on commanding.

A critical second component of this data stream is the reject event and good event counters, which are used to determine the deadtime of the instrument and convert the primary science data into absolute fluxes during periods of intense SEP radiation. Event counters, detailed below, are all 16-bit counters that "freeze" at the maximum count until reset. Every second the current-count value is transferred to a holding register (which is inserted into the secondary science telemetry) and the counter is cleared.

- The **reject event counter** is a 16-bit counter that is clocked every time an event is rejected by the discriminator accept mask test.

- The **good event counter** is a 16-bit counter that is clocked every time a qualifying event is processed. This counter is clocked for all events, even if they are not written into static random access memory (SRAM), due to buffer overflow, or read-out of SRAM the following second (telemetry overflow).

- The **total event counter** is simply the sum of the reject and good event counters; it is provided for data processing convenience.

- The **singles counters f**or each detector is a 16-bit counter that is clocked by the "Singles Count" signals received from the analog electronics subsystem. Since these inputs are asynchronous, they are sampled and filtered. Singles "incidents" with pulse widths <~ 200ns may not be recognized. Threshold energies for the singles counters are approximately 110 keV for the thin detectors and approximately 35 keV for the thick detectors.

3.3.4 Instrument Housekeeping

Instrument housekeeping packets are read every 16 seconds whenever 28VDC power is supplied to the instrument. The following describes the variables monitored in the housekeeping data stream.

Variables Monitored

Bias Voltages: The thin and thick detector bias voltages are recorded.

Temperatures: Temperatures recorded include the telescope electronics board, instrument chassis bulkhead, the APB, the DPB, and the DC/DC converters.

Total Dose: The APB board will contain a device for measuring the total radiation dose experienced by the electronics on the APB board. The device provides three analog outputs which are converted by the DPB into a 24-bit counter, the minimum step size of which is 0.020 mRad, and full scale reading of 335 Rad. The counter wraps after reaching full scale.

Currents: The detector leakage currents will be monitored for each individual thin and thick detector. For the thin detectors the monitor will cover the current range from 0-0.24 µA. For the thick detectors the monitor will cover the range from 0-0.12 µA.

3.3.5 Commands

The spacecraft provides a time-of-next interval command every second which is used to uniquely time-tag each telemetry packet. Commands available via ground command include:

- LLD levels (described above)
- Internal pulser calibration signal amplitude and rate
- Detector bias enable
- Individual detector processing enable/disable inputs
- Coincidence mask settings to define "good" events

3.3.6 Observation Strategy

Due to CRaTER's immovable mounting to the spacecraft (see Figures 14 and 15), telescope orientation is determined by the pointing of the LRO spacecraft. CRaTER is aligned, along with most other instruments on the spacecraft, with its telescope axis along the nadir/zenith line. As such, one of CRaTER's apertures (D6 end) will nominally be pointing towards the Moon, and the other towards deep

space (D1 end). Some excursions from this pointing, including limb sounding yaws in the +/- y-axis directions, are expected for brief periods for calibration and secondary science activities.

CRaTER's nominal measurement configuration will be to accept any detector coincidences as valid events, and, both the thin and thick detector LLD settings will be placed just above the noise. With the usual expected flux of particles that are measurable by CRaTER, this will allow us to analyze every valid detected event. In periods of high particle flux, the LLD settings will be adjusted to suppress the more dominant proton population in order to devote a higher percentage of our telemetry to the higher LET heavy ion population.

Section 3.1.2 examined the maximum fluxes expected in the D2 detector (Figure 6) due to the largest SEP events of the previous solar cycles. During these large events, the effects of the enhanced heavy ion spectrum may be more important scientifically than just measuring primarily the proton spectrum. Several features have been incorporated into the CRaTER signal processing design to allow for a reduction in the sensitivity of the instrument to SEP protons in favor of the rarer heavy ions. First, the thickness and LET ranges of the thin and thick detectors have been optimized such that the thin detectors that measure high LET events do not see many of the protons.   Furthermore, the FPGA is designed to be able to deactivate one or more of the detector signals for triggering a PHA by exceeding the LLD value. The LRO spacecraft monitors CRaTER secondary science event rates in real-time and is designed to reconfigure instrument settings accordingly within seconds.

The following describes the automated process that configures the instrument into three different operating modes depending on detection rates: low, elevated, and extreme. In the default "low rate" operating mode all events are sent to the ground; all detectors are in operation and the LLD thresholds for the thin and thick detectors are set just sufficiently high to avoid detector noise levels but otherwise are low. Once the event rate exceeds a certain value, the instrument switches automatically into an "elevated rate" mode, requiring at least two detectors to have detected a signal to record and telemeter a valid event. In the "extreme rate" case, the zenith-facing thick detector is disabled, the thin detector thresholds are raised above the signal level produced by protons, and detection is required by at least two of the enabled detectors. Mode switching can occur at a 60-second cadence and the mode is recorded in the telemetry stream.

This process will help ensure continued measurement of higher energy protons and all heavy-ion particles during the infrequent periods when the instrument response would otherwise become saturated by lower energy protons in its nominal configuration. During these times, the lowest LET portion of the spectrum (less than a few keV/micron) dominated by the protons is sacrificed in favor of the higher LET portions contributed by the heavy ions. The threshold event rates for mode transitions are reconfigurable through ground command.

4 Instrument Testing, Characterization, and Calibration

The purpose of this section is to describe the testing, characterization, and calibration of the CRaTER Flight Models (FM), based on lessons learned from experiences with the extremely high-fidelity Engineering Model (EM). In brief, considerable bench testing demonstrates that there is a desirable linear relationship between the digital value returned by the PHA and the original energy deposited in the detector. Gains and offsets for each detector are determined with high precision by calibrating the instrument with a beam of high energy protons produced by the Northeast Proton Therapy Center (NPTC) of Massachusetts General Hospital (MGH). A 230 MeV proton beam at the MGH NPTC (Cascio et al., 2003) is degraded in energy using sheets of plastic (Cascio et al., 2004) until a beam is produced with large energy dispersion and a peak energy tuned to the response of a pair of thin and thick detectors. The dispersed beam produces a characteristic track in energy deposition in the pair of detectors. The gains and offsets for each of the detectors is then determined by iteratively varying the free parameters of the instrument response until the measurements match the predictions of GEANT numerical simulations of the energy loss.

4.1 Instrument Characterization

4.1.1 Linearity of the Pulse Shaping

The most significant concern in instrument characterization is quantitatively understanding the relationship between the value of the energy deposited in the i-th detector and the resulting value produced by the ADC of the PHA. This relationship is demonstrated to be linear with an RMS residual of less than 0.1% using a stable external pulse generator. The external pulse generator is capable of generating stable, linear, and repeatable test pulses. A coaxial cable connects the pulse generator to any of the detector measurement chains before pre-amplification through a set of six connectors mounted directly on the telescope electronics board. An absolute scale for the external pulse generator is set using a series of attenuators and a coarse gain. Once the absolute scale is set a dial is used to generate pulse amplitudes with fractional amplitude variability of 0.01%.

We measured the height of the pulses generated by the external pulser and the best fit of a line to these data has an offset of 0.001 V, or approximately 0.03% of the peak value. The RMS of the residual to the linear fit is on the order 0.1%. It is important to note that both the small offset of 0.03% and the RMS residual from a linear relationship of 0.1% are upper limits imposed by the resolution of the sampling technique, and it is likely that the external pulse generator has even better performance. Nonetheless, these extremely low values are sufficient for our calibration needs.

Once we verified that the external pulse generator was linear, we connected it to each of the analog measurement circuits of the FM. The absolute amplitude of the external pulser was then set so that when the pulser amplitude dial was set to 1000 the resulting pulses just saturated the PHA. We then collected two minutes of data running at 100 events/second at each of nine input pulse amplitudes

spaced between 100 and 850. The returned events were then analyzed and the PHAs at each pulser amplitude were characterized as a Gaussian distribution with a width and a center. Figure 16 is a plot of the center channel of the measured peak, in analog-to-digital units (ADU),) as a function of pulser amplitude setting for all detectors in the FM. (The peak values for D1 are as measured; a successive offset of 100 ADU has been added so that the individual traces of D2 through D6 can be identified more clearly.) The relationship between pulser amplitude and measured peak is remarkably linear in each of the six detectors. Additional analysis, including finer pulser setting increments (not shown here), was used to quantify the linearity of the relationship, with the quadratic term only contributing ~0.3% at the highest values. The RMS residual from a simple linear model was significantly less that 0.1%. Since it is highly unlikely that the external pulse generator and the internal analog pulse shaping and PHA circuits would conspire to produce this linear agreement, we conclude that the relationship between E_i and C_i is also described with a linear relationship. Therefore, for the purpose of calibrating CRaTER at the accuracy required for the success of the mission, we may write,

$$E_i = G_i(C_i - O_i) \quad [keV]$$

where G_i $[keV\ ADU^{-1}]$ is the gain of the i-th detector chain and O_i $[ADU]$ is its zero offset.

4.1.2   Electronics Noise Level

The number of samples collected at each pulser setting permits examination and determination of an upper limit on the electronics noise level. Figure 17 is a plot of the standard deviations of the pulse height distribution as a function of the mean of each distribution for a range of pulse amplitudes. These measurements were taken with the instrument operating in a refrigerator held at 10°C, a temperature representative of typical in-flight values. Results are plotted for all six detectors of the FM. The width of the measured peak (in ADU) is clearly a linear function of the center of the measured peak (in ADU), or a fixed fraction of the peak amplitude. For these measurements the noise is approximately 0.15% of the amplitude, well below the maximum noise level requirement. However, it is important to note that the measured noise is a combination of the noise in the pulse shaping and PHA circuitry within the instrument and any noise produced by the external pulse generator itself. These measurements therefore are an upper limit on the true noise level of the CRaTER analog electronics of 1 ADU or 0.02% of the maximum energy, far below levels needed to achieve our measurement requirements.

4.1.3   Stability

While the internal pulse generation system is mainly used for verifying instrument functionality and not for precise calibration purposes, it is useful for tracking CRaTER's stability over time. Each time the FM went into testing it was customary to conduct a full sweep through all of the possible amplitudes of the internal calibration system. Figure 18 is a plot of the measured center peak in each of the six FM detectors to a fixed internal pulse as a function of time.   Five internal calibration runs span a period of

approximately 18 months. Variation in the response over this period, taken under different operating situations and at different locations, remains stable at the ~0.06% level.

4.1.4   Temperature Dependence

The temperature dependence of the CRaTER electronics was determined by placing the instrument in a thermal chamber while feeding pulses through the chamber wall from the external pulse generator, which is maintained at room temperature. Figure 19 is a plot of the response of each detector chain to a fixed external amplitude pulse over the entire expected operating temperature range of the instrument. The gain has a very weak and non-linear dependence on temperature. However, note that over the entire temperature range, the total variation is only approximately ±0.1% for the thick detectors and ±0.5% for the thin detectors. We conclude that the thermal dependence of the instrument response is very small, on the order of <0.5% level effect, and that a simple temperature-dependent function describes the thick and thin detector gains sufficiently well.

4.2   Theory and Modeling

This section provides the theoretical basis for our ability to characterize CRaTER using a spread beam of protons. Figure 20 is a plot of the typical energy deposited into the components of CRaTER as a function of initial energy for a beam of protons. This calculation was performed by creating a table of typical energy loss rate as a function of energy for protons in silicon using the SRIM program. Note that the maximum energy deposited is by a particle that just stops at the back of the detector. The thicker detector can therefore produce a larger energy deposit of slightly more than 10 MeV, compared to the ~4 MeV of the thin detector. Once the particle has enough energy to pass through the detector, the total energy deposited decreases as the particle's energy loss rate decreases.

In reality, the situation is more complex than the relations shown in Figure 20. This is because the SRIM code only describes proton energy loss in a statistical sense. It also does not include physics such as nuclear interactions, deep inelastic scattering, and other interactions such as pion production. GEANT4 is a more sophisticated toolkit for the simulation of the passage of particles through matter with an abundant set of physics processes to handle diverse interactions of particles with matter over a wide energy range. For many physics processes a choice of different models is available, and overall the results are much more realistic than the simple SRIM calculations. Figure 21 is similar to Figure 20, but it has been generated using GEANT4 and shows energy depositions in the first pair of detectors. GEANT4 is used extensively in the community, and is especially well-validated at proton energies relevant to CRaTER measurements for calibration.

Figure 22 shows a two dimensional histogram of simulated energy deposits measured in, for example, detectors D3 (thin) and D4 (thick) expected from a normally incident beam of protons with a uniform distribution of energy, using GEANT4 and the actual CRaTER detector thicknesses and materials.

For this figure, only particles that produced a simulated signal in both virtual detectors were included in the histogram. The vertical dashed line indicates the simulated D3 LLD threshold. Five key portions of the histogram are labeled, and represent the track that proton energy deposition follows as a function of increasing incident proton energy : (1) protons pass into and stop in D3; (2) protons just stop in D3; (3) protons make it farther into D4 with increasing energy; (4) protons just stop in D4; (5) protons pass through D4. This strongly characteristic pattern is produced in each thin-thick detector pair at energies at and near the point where protons are just stopping in a particular detector. The encircled locations are these key locations in energy space. We use this characteristic signature as the theoretical basis in the end-to-end calibration procedure described next.

4.3   Calibration

Final calibration of the CRaTER Flight Models (FM) was based on lessons learned from extensive experiences developed with the high-fidelity, flight-like Engineering Model (EM). Techniques developed with the EM were refined and applied to the FM before instrument delivery.   In brief and as designed, there exists a straightforward linear relationship between the digitized value returned by the PHA system (ADU) and the original energy deposited in the detector (keV).

Calibration consists of two major activities. In addition to an end-to-end calibration conducted on the fully integrated flight model (described below), laboratory testing of individual detector chains provided an independent, first-level of calibration. Before and during final assembly of the telescope, radionuclides such as Cobalt-60 and Americium-241 stimulate each detector chain while in vacuum. These sources produce well-defined particle and/or photon energies, which along with an external, high-precision pulse generator, provide a means to establish quantitatively the ultimate association between detected energy and ADU value.   Once fully integrated, individual detectors can no longer be stimulated by particles from radionuclides.   Therefore, a second stage of calibration for the fully-integrated CRaTER instrument complements the sub-system calibrations.

Final system gains and offsets for each detector are determined with high precision by calibrating the instrument with a beam of high energy protons produced by the Northeast Proton Therapy Center (NPTC) of Massachusetts General Hospital. A well-calibrated 230 MeV proton beam at MGH is degraded in energy using sheets of plastic until a beam is produced with large energy dispersion and a peak energy tuned to the characteristic energy deposition response of a pair of thin and thick detectors (shown above in Figure 22).   Since we have previously shown that the relationship between the energy deposited in a detector and the channel number determined by our measurement chain is a simple linear function, the absolute response of each detector in the instrument can be determined. The gains and offsets for each of the detectors are determined by iteratively varying free parameters of the instrument response until the measurements match the predictions of GEANT4 numerical simulations of the energy loss.

The experimenter's beamline at the MGH proton facility has its own dedicated target room designed not for medical patients but rather for physics experiments. The geometry of the beam line for a typical CRaTER beam test is shown in Figure 23. The beam is transported under vacuum and exits through a Kapton window (from the far right). There is a collimator just downstream of this window to allow precise positioning of apertures, beam degraders, and any sensing devices, including CRaTER. Alignment is provided with a laser system, and the distance between the window and the collimator is typically 90 cm. The equipment area is shielded, and experience has shown the shielding to be adequate to keep neutron doses low enough to avoid harming electrical equipment in the vicinity of the test device.

A primary population of 230 MeV protons is generated by an upstream cyclotron. After emerging from this cyclotron, the protons are degraded in energy by a rotating carbon wedge. Magnetic selection allows the user to define momentum and emittance. In this way the user can obtain monoenergetic beams from 70 through 230 MeV.

Dosimetry is provided by the insertion of a thin-foil ion chamber upstream of the instrument under test. This chamber is calibrated to fluence or dose by a Faraday cup, a thimble ion chamber, or a radiation sensitive diode placed at the target location. This calibration is normally done just prior to measurements. The ion chamber is set up to send information about flux and total dosage in real time to monitoring devices located in the control room.

The most commonly employed energies are 160 and 230 MeV. The 160 MeV configuration allows currents to 15 nA, while 230 MeV allows currents of 80 nA. In all cases these currents can be stepped down with energy degraders. Small diameter beams - less than 1 cm - or targets where uniformity is not crucial use the unscattered beam spot directly from the cyclotron. Medium diameter beams - from 1 to 5 cm - use a single scatterer to get a Gaussian spatial distribution of the right size and then employ a collimator to produce a central flat region. Medium diameter beams - from 1 to 5 cm - use a double scattering arrangement. The second scatterer is contoured to use incident protons efficiently, and allows beams to 20 cm. All beams make a circular spot, though this can be changed with custom collimators.

During beam testing at MGH, the CRaTER unit is mounted on a tripod so the telescope is within the beam line. The 1 Hz clock, DC power supply, and 1553 ground support equipment (GSE) interface are placed behind a wall to shield them from the radiation present within the room when the beam is operating. A router in the office connects the GSE to the wireless local area network, permitting computers in the office to command the instrument, record returned telemetry to the permanent archive, and display scientific data in real time.

The calibration procedure is as follows. First, a simulated PHA 2D histogram is generated by using the best guess calibration free parameters to convert simulated deposited energies into ADC channels. GEANT4 is used along with a high-fidelity model of the CRaTER detectors for this purpose. A full simulated response is created by generating synthetic histograms over a range of incident energies and then integrating over the histograms with weighting determined by the initial best guess for the

beam center energy and width. The simulation is compared with the observations and the free parameters (gain and offset) are adjusted until the model converges with the observations. We begin by selecting all of the beam data that produced a signal in both of the detectors for a given detector pair. A 2D histogram is then generated, with histogram intervals varied appropriately to achieve good resolution of the proton trajectory traced out in the histogram. An initial guess is then made for the beam parameters along with the free parameters of the instrument response model. The important free parameters fixed by this calibration technique are the detector gains and the energy offsets.

An example of an iteration step is shown in Figure 24. The top panel displays a histogram of energy deposits (expressed in ADU) in D3 (horizontal axis) and D4 (vertical axis). The color coding indicates the number of energy deposits at each point in the two-dimensional histogram (purple is the zero level background, ranging to red at the highest level). The bottom panel displays a histogram of the comparable two-dimensional histogram as predicted by the GEANT4 model incorporating all the key geometries and materials of the detectors under calibration. At each step in the iterative process, detector gains and energy offsets needed to convert from modeled absolute energy to ADU are recorded. The best fit solution yields final calibration values.

As-delivered calibration values determined from the sub-system and full calibration process on the flight model are shown in Table 6. These values provide the means to convert digital values of pulse-height in each detector to the energy deposited in each detector, a key step needed to estimate LET. Ever more definitive calibration coefficients continue to be refined through ongoing analysis of extant data; definitive values will be updated as part of the formal delivery of CRaTER data to NASA's Planetary Data System archive.

In addition to this final calibration process, the CRaTER EM instrument response was characterized further at the NASA Space Radiation Laboratory (NSRL) at Brookhaven National Lab (BNL). While these beam runs did not contribute directly to establishing final calibration coefficients for the FM, they did provide another critically important data source for establishing instrument response over the full range of LET we can expect in space. The BNL NSRL facility is ideal for this purpose as it is designed for simulating the heavy ion component of GCR which produces inherently high LET response, in addition to protons. Instrument characterization runs at BNL included: protons, silicon, iron, and chlorine ions at various energies between <300 and 1000 MeV/nucleon. The results from these CRaTER runs and comparison with models have already been published (Charara, 2008) and are the focus of future publications.

5   Data Analysis, Interpretation, and Modeling

The CRaTER Science Operations Center (SOC) is located in Boston University's Astronomy Department, part of the University's Charles River Campus. The SOC's main function is to receive process, display, archive and distribute data from the CRaTER instrument and the ancillary spacecraft engineering and positional information necessary for a more detailed analysis of the data. The basic

architecture of the CRaTER SOC is shown in Figure 25. The SOC's core consists of two independent sets of secure Linux-based workstations and a RAID-based data archive. Within each set are two identical machines—a prime and backup—to provide a mechanism for rapid recovery in the case of hardware failure. Both sets are part of the Boston University network domain (bu.edu).

The first set, designated SOC-A/SOC-B, receives the real-time telemetry stream, instrument data files, and ancillary flight data files and other products produced by the LRO Mission Operations Center (MOC). The SOC-A/SOC-B computers host the CRaTER data pipeline process—a set of scripts and software that convert the data in the instrument data and housekeeping files from binary to ASCII format, apply calibration and engineering conversion factors, perform data quality checks, and merge the data with corresponding spacecraft ephemeris and pointing data. Copies of all the received files and pipeline process products are stored in a local archive on the RAID array. Every three months, beginning six months following the end of the initial mission commissioning period, the most recent three months of flight data files, MOC products, and pipeline process products, are assembled into an archive and submitted to NASA's Planetary Data System's (PDS's) Planetary Plasma Interactions (PPI) data archive node.

Starting from the Level 0 data, the CRaTER SOC will develop and deliver higher level data products to the UCLA node of the Planetary Data System. The Level 0 and higher order data products are all directly related to the primary CRaTER measurement: the LET in six silicon detectors embedded within the TEP telescope. The pipeline flow from raw data to Level 2 data delivered to the PDS, including the description of each data product, is shown in Figure 26. In addition, NASA/JSC's Space Radiation Analysis Group and NOAA's Space Weather Prediction Center contributed significantly to defining tailored data products to support astronaut operations and space weather customers. For example, higher-level, user-motivated data products will include estimates of "surface", "tissue", and "deep tissue" dose and dose rates in near real-time over the course of the LRO mission.

The Monte Carlo transport code HETC-HEDS (Townsend, et al, 2005) is used to model the anticipated radiation environment at the Moon during the LRO mission (Charara, 2008). Initially, the code was used to perform benchmarking studies of the simulations by comparing them to measurements from CRaTER calibrations performed with proton beams from the cyclotron at Massachusetts General Hospital, and various heavy ion beams at the NASA Space Radiation Laboratory at Brookhaven National Laboratory. Next, an LET database that includes simulations of all the relevant components of the GCR spectrum with their corresponding energies was generated for the CRaTER flight model configuration. Particles with charges between $1 \leq Z \leq 26$ (protons through iron) and kinetic energies between 20 MeV per nucleon and 3 GeV/nucleon were used for these simulations (Particles heavier than iron have fluences that are too low to be of practical concern for radiation protection purposes). Then estimates of total energy lost per path length of material by any particle produced, whether it is a primary beam particle or a secondary particle generated from a fragmentation event from the projectile or the target are used to obtain an average LET for each particle type, energy and detector component. The complete LET data base for these GCR elements (protons through iron) was developed for use by the CRaTER team for future analyses of, and comparisons with, real time data obtained with CRaTER during the actual mission.

Specific HETC-HEDS model predictions of the expected LET spectrum from the anticipated GCR environment during the mission time frame (2009-2010) have been made and are available for prompt comparison with the measured LET spectrum for the mission. The response of the detector to various historical SEP spectra from 1989 and 2003 have also been simulated with HETC-HEDS using the measured spectra from those events. For instance, a large event (November 1997) that occurred during the comparable phase of the previous solar cycle, was modeled as an example of a solar energetic particle event that might occur during the prime or extended mission phases. Finally, theoretical calculations of the level of nuclear interactions that will occur within the TEP and other elements of the telescope, along with observations of fragmentation collected both on the ground at heavy ion accelerators and ultimately at the Moon, will be the subject of separate publications.

6   Discussion and Summary

6.1   Other Representative Science Goals

In addition to its exploration-enabling measurements of the lunar radiation environment, CRaTER also provides high-quality observations which in turn enables many other scientific investigations. While not the primary goal of the LRO mission during its primary phase, these areas serve as secondary science goals during the first year of operations and targeted science topics for any extended mission scenarios. Several example science studies using CRaTER measurements follow next.

6.1.1   Lunar-Plasma Environment Interactions

The Moon is electrostatically charged by the surrounding space plasma environment, including the spatially-varying regions of hot plasma within the Earth's distant magnetotail (Spence and Kivelson, 1990) and time-varying solar wind plasma in and near the lunar wake (Clack et al., 2004), as well as by solar ultraviolet (UV) radiation. Observations from Lunar Prospector indicate that during SEP events the shadowed lunar surface can charge up to a few kilovolts negative when the Moon is in the solar wind or the plasma sheet region of the magnetotail (Halekas et al., 2007). Even during less extreme conditions, it is likely that strong local electric fields can form on the lunar surface, particularly near the terminator and in the polar regions, which could drive the transport of charged lunar dust (e.g., see Colwell et al., 2007). There is evidence to suggest that a submicron dust population exists in the lunar exosphere at altitudes in excess of 100 km (Zook and McCoy, 1991), and it has been proposed that this population could have been electrostatically lofted by surface electric fields (Stubbs et al., 2006). However, lunar surface charging and dust transport processes remain poorly characterized and understood. In addition to the intrinsic scientific interest of such processes, these environmental factors and their dynamics will

likely pose a hazard to human and robotic explorers, thereby further motivating and justifying their scientific study (Stubbs et al., 2007).

By using CRaTER and other LRO instruments and spacecraft capabilities (including off-nadir pointing) we will perform the following studies of the exospheric dust environment around the Moon. We will analyze and interpret any CRaTER signals suspected to have been generated by microphonics produced by direct meteoritic or exospheric dust impacts. When pointing off-nadir, we will analyze and interpret secondaries that were likely created by GCR and SEP spallation from exosphere dust. If exospheric dust is detected, then CRaTER data could help place important limits on its spatial and temporal mass distribution.

6.1.2   Sources of Galactic Cosmic Ray Variability

Galactic cosmic rays represent a low-level but continuous source of very energetic charged particles which bathe the solar system. Earth-based measurements reveal variability of GCR that range from the well-known solar cycle timescales (11 and 22-year), to partly understood intermediate timescales associated with solar rotation, corotating interaction regions and Forbush decreases (days), to nearly completely unexplored short timescales (hours and less).

Recent high-time-resolution measurements of GCR taken beyond Earth's shielding magnetic field and protective atmosphere have demonstrated that new physical understanding of the intermediate and short timescale variations are possible (c.f., Quenby et al, 2008; Mulligan et al., 2009). These recent studies have been accomplished with instruments designed principally for other measurements, rather than instruments dedicated to cosmic rays. CRaTER therefore represents an important and highly capable scientific instrument that will provide important new insights on GCR variability. Specific topics that we expect to address with CRaTER observations include: comparison of present solar minimum GCR with past cycles and its variability toward solar maximum; exploration of substructure observed in Forbush decreases and the possible role that planar magnetic structures might play in modulating GCR flux (Jordan et al., 2009); and characterizing GCR "scintillation" (Owens and Jokipii, 1973) and assessing the source of such variability. Finally, we will quantify the degree to which any measurable shielding of >10 MeV ions is provided by the terrestrial magnetosphere as a function of lunar orbit phase and compare with recent contrasting predictions suggested by Winglee and Harnett (2007) and challenged by Huang et al. (2009)

6.1.3   Solar Proton Studies

Intense solar proton events are episodic and approximately follow the solar cycle. In addition to being a second source of ionizing radiation risks, the structure and dynamics of SEPs have intrinsic scientific interest. SEPs represent a population of particles with typically power-law spectra up to 100's of MeV/nucleon that occassionally are accelerated to near the speed of light in explosive solar phenomena, including shock waves in the solar corona associated with flares, and shock waves in the interplanetary medium associated with coronal mass ejections as they propagate into the heliosphere (e.g., Cane and Lario, 2006; Mewaldt, 2006). A major challenge with SEPs is predicting their arrival time, which is often tied intimately to predicting the arrival time of interplanetary shocks (Case et al., 2008). Solar protons thereby are tracers of particle acceleration as well as their transport mechanisms (field-aligned transport versus cross-field diffusion) that allow them to arrive at any given location in the heliosphere from their source location.

CRaTER will provide high time-resolution measurements of SEPs which, combined with other simultaneous heliospheric measurements at multiple locations, can be used to probe these processes and mechanisms in new ways. SEP topics that we will study include: temporal (spatial) structure of SEP onset , dispersionless high-time resolution SEP drop-outs, and time-of-flight energy dependence of SEPs for particle acceleration and transport identification (c.f., Mazur et al., 2000).

6.1.4   Exploring Surface Interactions with Secondaries

Though never a primary science driver, we nevertheless hope to exploit the as-designed capabilities of CRaTER in order to perform off-nadir measurements to explore possible lunar surface interactions with GCR. GCR with sufficiently high energies and incident with the lunar surface particularly at near grazing incidence can produce secondary by-products through spallation which may be detected at the LRO orbit. Radiation transport codes show that the relative population of secondaries depend upon the properties of the surface material being spallated. This process could be used to remotely sense some aspects of the surface using the lunar albedo, with the charged secondaries or neutrons (c.f., Adams et al., 2007). This is a purely exploratory measurement we will do during the commissioning phase and periodically during the main mission. Though this is a speculative measurement, we would look for any potentially small signal against the GCR and SEP foregrounds by looking not only at rate effects, but also tell-tale features in the LET spectra.

6.1.5   Comparative Studies of Lunar and Martian Radiation Environment

Comparison of simultaneous measurements of the radiation environment at the Moon and at Mars can be used to study the processes which modify GCR and SEP fluxes throughout the inner heliosphere. SEPS in particular are of interest for such studies; their arrival and time history depends critically on magnetic connection to particle acceleration regions and the detailed propagation of shocks

through the heliosphere. Data from CRaTER will be combined with data from the ongoing Mars Odyssey and upcoming Mars Science Lander missions, as available. On Odyssey (Saunders et al., 2004), even though MARIE is no longer functional, other instruments are working and provide integral charged particle fluxes, including the GRS instrument. Though designed primarily to measure gamma rays, the GRS instrument has provided a near-continuous record of GCR and SEP flux in the Martian orbit from 2002 to present. The Odyssey HEND instrument measures high-energy neutrons, a proxy for solar protons during SEPs. In addition to currently available Odyssey observations, we anticipate similar comparison opportunities with radiation measurements from the RAD instrument planned for the Mars Science Lander. During the prime mission, Mars and Earth will not be particularly well-aligned to study solar proton transport and connectivity. However, comparison of LRO measurements to Mars data may be more interesting during an extended mission period, especially if SEP's are observed when the Moon and Mars are approximately connected magnetically by the large-scale interplanetary magnetic field.

6.2   Summary

The Cosmic Ray Telescope for the Effects of Radiation (CRaTER) on the Lunar Reconnaissance Orbiter (LRO) characterizes the lunar radiation environment by quantifying the evolving LET spectrum through different amounts of TEP owing to GCR and SEP particle populations. By characterizing energy loss from the interactions of biologically-relevant ions with energies above ~10 MeV, CRaTER LET measurements serve as in-flight constraints needed to validate state-of-the-art radiation transport codes. In addition to these human exploration goals, CRaTER measurements also provide new windows on the science of SEP and GCR phenomena and their interactions with the lunar surface.

7   Acknowledgments

Instrument Manager Arlin Bartels; we are grateful to have had such a professional and dedicated instrument manager who made the entire process minimally troublesome and nearly exclusively joyous from instrument concept to launch. Finally, we gratefully acknowledge the unique contributions of Ann Vasaly, of the Classics Department at Boston University, who helped us develop the Latin motto for CRaTER, which is: "Luna Ut Nos Animalia Tueri Experiri Possimus" ("In order that we might be able to protect and make trial of living things on the Moon").

8 References

Adams, J. H., M. Bhattacharya, Z.W. Lin, G. Pendleton, J.W. Watts. "The ionizing radiation environment on the moon." Advances in Space Research 40, 338–341, 2007.

Badhwar, G.D., M. J. Golightly, A. Konradi et al., In-flight radiation measurements on STS-60, Radiation Measurements, 26(1), 17-34, 1996.

Blake, J. B., J. F. Fennell, L. M. Friesen, B. M. Johnson, W. A. Kolasinski, D. J. Mabry, J. V. Osborn, S. H. Penzin, E. R. Schnauss, H. E. Spence, D. N. Baker, R. Belian, T. A. Fritz, W. Ford, B. Laubscher, R. Stiglich, R. A. Baraze, M. F. Hilsenrath, W. L. Imhof, J. R. Kilner, J. Mobilia, H. D. Voss, A. Korth, M. Güll, K. Fischer, M. Grande, and D. Hall, CEPPAD: Comprehensive Energetic Particle and Pitch Angle Distribution Experiment on POLAR, Space Sci. Rev., 71, 531, 1995.

Cane, H. V., and D. Lario, An Introduction to CMEs and Energetic Particles, Space Sci. Rev., 123, p 45-56, 2006.

Case, A. W., H. E. Spence, M. J. Owens, P. Riley, and D. Odstrcil (2008), Ambient solar wind's effect on ICME transit times, Geophys. Res. Lett., 35, L15105, doi:10.1029/2008GL034493.

Cascio, E., W. J.. M. Sisterson, J. B. Flanz, and M.. S. Wagner, The Proton Irradiation Program at the Northeast Proton Therapy Center, NSREC Proceedings, 2003.

Cascio, E. W., J. M. Sisterson, B. Gottschalk, and S. Sarkar, Measurements of the Energy Spectrum of Degraded Proton Beams at NPTC, NSREC Proceedings, 2004.

Charara, Y. M.: Characterization of the Cosmic Ray Telescope for the Effects of Radiation (CRaTER) Detector. Ph.D. Dissertation, The University of Tennessee, Knoxville, Tennessee, December 2008.

Clack D, J. C. Kasper, A. J., Lazarus, J. T. Steinberg, and WM Farrell, Wind observations of extreme ion temperature anisotropies in the lunar wake, Geophys. Res. Lett., 31, 6, 2004.

Colwell, J. E., S. Batiste, M. Horányi, S. Robertson, and S. Sture (2007), Lunar surface: Dust dynamics and regolith mechanics, *Rev. Geophys.*, 45, RG2006, doi:10.1029/2005RG000184.

Golightly, M. J., K. Hardy, and W. Quam, Radiation-dosimetry measurements during US space-shuttle missions with the RME-III, Radiation Measurements, 23(1), 25-42, 1994.

Halekas, J. S., G. T. Delory, D. A. Brain, R. P. Lin, M. O. Fillingim, C. O. Lee, R. A. Mewaldt, T. J. Stubbs, W. M. Farrell, and M. K. Hudson (2007), Extreme lunar surface charging during solar energetic particle events, Geophys. Res. Lett., 34, L02111, doi:10.1029/2006GL028517.

Huang, C.-L., H. E. Spence, and B. T. Kress, Assessing access of galactic cosmic rays at Moon's orbit, Geophys. Res. Lett., 36, L09109, doi:10.1029/2009GL037916. 2009.

Jordan, A. J., H. E. Spence, J. B. Blake, T. Mulligan, D. Shaul, M. Galametz, Multipoint, High Time Resolution Galactic Cosmic Ray Observations Associated With Two Interplanetary Coronal Mass Ejections, J. Geophys. Res., 114, A07107, doi:10.1029/2008JA013891., 2009.

Kim, Y., J. W. Wilson, S. A. Thibeault, J. E. Nealy, F. F. Badavi, and R. L. Kiefer, Performance Study of Galactic Cosmic Ray Shield Materials, NASA Technical Paper 3473, November 1994.

Luhmann, J G., et al., STEREO IMPACT Investigation Goals, Measurements, and Data Products Overview, Space Sci. Rev., 136, 117-184, 2007.

Mazur, J. E., Mason, G. M., Dwyer, J. R., Giacalone, J., Jokipii, J. R. and Stone, E. C. (2000), Interplanetary Magnetic Field Line Mixing Deduced from Impulsive Solar Flare Particles, Astrophys. J. 532, L79, 2000.

Mewaldt, R. A., Solar Energetic Particle Composition, Energy Spectra, and Space Weather, Space Sci. Rev., 124, p 303-316, 2006.

Mitrofanov et al., Lunar Exploration Neutron Detector for NASA'S Lunar Reconnaissance Orbiter Project, Space Sci. Rev., this issue, 2009.

Mulligan T., J. B. Blake, D. Shaul, J. J. Quenby, R. A. Leske, R. A. Mewaldt, M. Galametz, Short-period variability in the galactic cosmic ray intensity: High statistical resolution observations and interpretation around the time of a Forbush decrease in August 2006, J. Geophys. Res., 114, A07105, doi:10.1029/2008JA013783., 2009.

NASA Life Sciences Division Technical Report, "Strategic Program Plan for Space Radiation Health Research" Life Sciences Division, Office of Life and Microgravity Sciences and Applications, National Aeronautics and Space Administration, Washington, D.C. 20546, 1998.

NASA "Bioastronautics Roadmap: A Risk Reduction Strategy for Human Space Exploration", NASA/SP–2004–6113, 2005.

Owens, A. J., and J. R. Jokipii, Interplanetary Scintillations of Cosmic Rays, 502 Astrophys. J., 181, L147–L150, 1973.

Quenby, J. J., T. Mulligan, J. B. Blake, J. E. Mazur, and D. Shaul (2008), Local and nonlocal geometry of interplanetary coronal mass ejections: Galactic cosmic ray (GCR) short-period variations and magnetic field modeling, J. Geophys. Res., 113, A10102, doi:10.1029/2007JA012849.

Saunders, R., R. Arvidson and G. Badhwar et al., 2001 Mars Odyssey mission summary, Space Sci. Rev. 110, pp. 1–36., 2004.

Spence, H. E., and M. G. Kivelson (1990), The variation of the plasma sheet polytropic index along the midnight meridian in a finite width tail, *Geophys. Res. Lett.*, 17(5), 591–594.

Stone, E. C. C. M. S. Cohen, W. R. Cook, A. C. Cummings, B. Gauld, et al., The Cosmic-Ray Isotope Spectrometer for the Advanced Composition Explorer, Space Sci. Rev., 86, 285-356, 1998.

Stubbs, T.J., R.R. Vondrak, and W.M. Farrell (2006), A dynamic fountain model for lunar dust, *Adv. Space Res.*, 37(1), 59–66.

Stubbs, T. J., R. R. Vondrak, and W. M. Farrell (2007), Impact of dust on lunar exploration, in Proceedings of Dust in Planetary Systems 2005, Eur. Space Agency Spec. Publ., edited by H. Kruger, and A. Graps,2007.

Townsend, L. W. , T. M. Miller, and Tony A. Gabriel, "HETC radiation transport code

development for cosmic ray shielding applications in space", Radiation Protection Dosimetry Vol. 116, No. 1-4, 135-139, 2005.

Webber, W. R., and J. A. Lezniak, The comparative spectra of cosmic-ray protons and helium nuclei, Astrophys. Sp. Sci., 30, 361-380, 1974.

Wilson, J.W., Badavi, F.F., Cucinotta, F.A., Shinn, J.L., Badhwar, G.D., Silberberg, R., Tsao, C.H., Townsend, L.W., Tripathi, R.K., 1995. HZETRN: Description of a free-space ion and nucleon transport and shielding computer program. NASA Technical Paper 3495, US Government Printing Office, Washington, DC.

Winglee, R. M., and E. M. Harnett, Radiation mitigation at the moon by the terrestrial magnetosphere, Geophysical Research Letters, 34, doi:/10.1029/2007GL030507, 2007.

Yao, W.-M. et al., Review of Particle Physics, Journal of Physics G: Nucl. Part. Phys. 33, 1-1232 doi: 10.1088/0954-3899/33/1/001, 2006.

Ziegler, J. F., J. P, Biersack, U. Littmark, The Stopping and Range of Ions in Solids, J. F. Vol. 1 ,"Stopping and Ranges of Ions in Matter," Pergamon Press, New York (1984).

Zook, H.A., J.E. McCoy (1991), Large scale lunar horizon glow and a high altitude lunar dust exosphere, *Geophys. Res. Lett.*, 18(11), 2117–2120.

9 Tables

Property	Value	Comments
Mass	5.53 kg	6.36 kg allocation
Power	6.66 W	9.00 W allocation
Maximum Telemetry Rate	89.1 Kbps	Sized for largest historic solar proton event
Maximum Event Transmission Rate	1200 events/sec	Event defined as pulse height analysis on all 6 detectors for any valid detection
Low LET Range	0.09 keV /µm to 85 keV/ µm	Determined with thick detectors (D2, D4, D6)
High LET Range	2.3 keV/ µm to 2.2 MeV /µm	Determined with thin detector (D1, D3, D5)
LET Resolution	<0.3% of maximum LET in each Range	Net RSS value including detector and electronics noise, and gain uncertainty
Minimum Geometric Factor	0.57 cm^{2}sr	Defined by D1-D6 geometry
Zenith Full Angle Field of View	31.4°	Defined by D1-D6 geometry
Nadir Full Angle Field of View	65.9°	Defined by D4-D6 geometry

Table 1. Summary of as-delivered CRaTER flight unit physical properties and measurement performance.

A-150 Tissue Equivalent Plastic (TEP)		
Element	Mass Composition (%)	Use for CRaTER (%)
H	10.33 ± 0.07	10.33
C	76.93 ± 0.09	76.93
N	3.30 ± 0.08	3.30
O	6.94 ± 0.51	6.93*
F	1.14 ± 0.60	1.14
Ca	1.37 ± 0.06	1.37
Total		93.07
Density	1.127 ± 0.005 g/cm³	1.127 g/cm³
TEP on-axis linear dimensions : 53.992 mm (zenith section) and 26.972 (nadir section)		
*O composition not measured--assumed to be the balance of the elemental composition		

Table 2: Composition of A-150 TEP used in CRaTER by mass.

Al 6061-T6		
Element	**Mass Composition (%)**	**Use for CRaTER (%)**
Al	95.8 - 98.6	97.200
Cr	0.0400 - 0.350	0.195
Cu	0.150 - 0.400	0.275
Fe	≤ 0.700	0.455
Mg	0.800 - 1.20	1.000
Mn	≤ 0.150	0.075
Si	0.400 - 0.800	0.600
Ti	≤ 0.150	0.075
Zn	≤ 0.250	0.125
Other, each	≤ 0.0500	
Other, total	≤ 0.150	
Total		*100.00*
Density	2.70 g/cm³	2.70 g/cm³
Aluminum end cap thickness : 812.8 μm (zenith cap) and 810.3 μm (nadir cap)		

Table 3: Composition and thickness of Al 6061-T6 aluminum endcaps used in CRaTER by mass.

Location	Material	Thickness (mm)	Cumulative Distance (mm)
S1	Aluminum	0.8128	0,8128
S1 (back) → D1 (front)	(void)	2.363	3.1758
D1	Silicon	0.148	3.3238
D1 (back) → D2 (front)	(void)	3.360	6.6383
D2	Silicon	1.000	7.6838
D2 (back) → T1 (front)	(void)	3.943	11.6268
A1	A-150	53.967	65.5938
A1 (back) → D3 (front)	(void)	3.554	69.1478
D3	Silicon	0.149	69.2968
D3 (back) → D4 (front)	(void)	3.568	72.8648
D4	Silicon	1.000	73.8648
D4 (back) → A2 (front)	(void)	11.900	85.7648
A2	A-150	26.980	112.7448
A2 (back) → D5 (front)	(void)	11.900	124.6448
D5	Silicon	0.149	124.7938
D5 (back) → D6 (front)	(void)	3.060	127.8538
D6	Silicon	1.000	128.8538
D6 (back) → S2 (back)	(void)	2.362	131.2158
S2	Aluminum	0.81026	132.0260

Table 4: Linear dimension of telescope components. Component designations are described fully in section 3.1.1; "S" refers to end cap shields, "D" refers to detectors, and "A" refers to A-150 TEP.

Representative Coincidences	Field of view (full angle)	Geometric factor (cm^2-sr)	Proton threshold energy (MeV)
D1·D2	169.0	24.152	12.7 (z)
D1·D4	53.4	1.679	90.8 (z)
D1·D6	31.4	0.569	114.5 (z)
D6·D5	170.0	24.566	17.7 (n)
D6·D4	65.9	2.564	63.9 (n)

Table 5: Fields-of-view, geometric factors, and threshold energies of representative coincidences

Parameter	Units	D1	D2	D3	D4	D5	D6
Thickness	Microns	148	1000	149	1000	149	1000
Gain, G_i	KeV/ADU	76.3	21.8	78.6	21.6	76.3	21.9
Offset, O_i	ADU	-0.4	-0.6	-0.3	-1.1	-0.1	-0.3

Table 6. As-delivered calibration values for the CRaTER flight model.

10 Figures
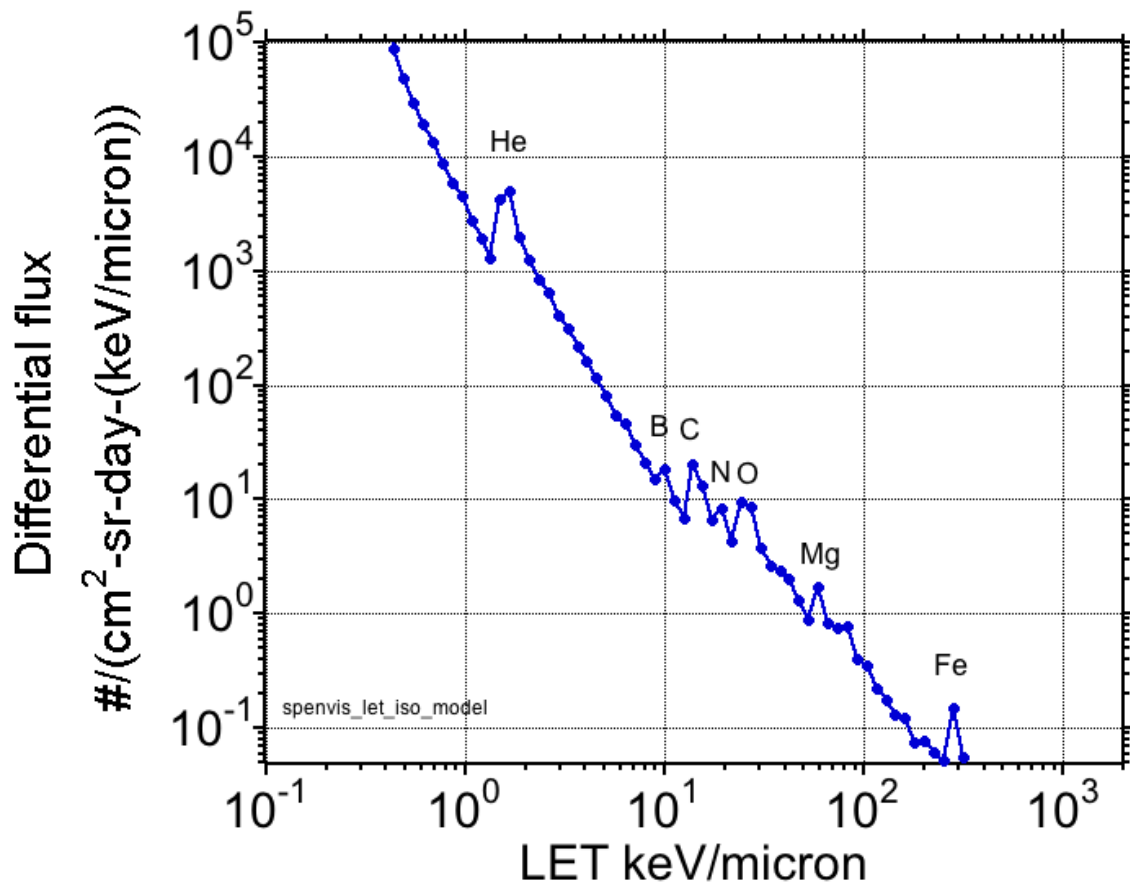
Figure 1. Modeled LET spectrum in silicon behind 1mm of aluminum using the CREME86 model and a galactic cosmic ray spectrum appropriate to the 1996 solar minimum, similar conditions to that expected during LRO's prime mission.
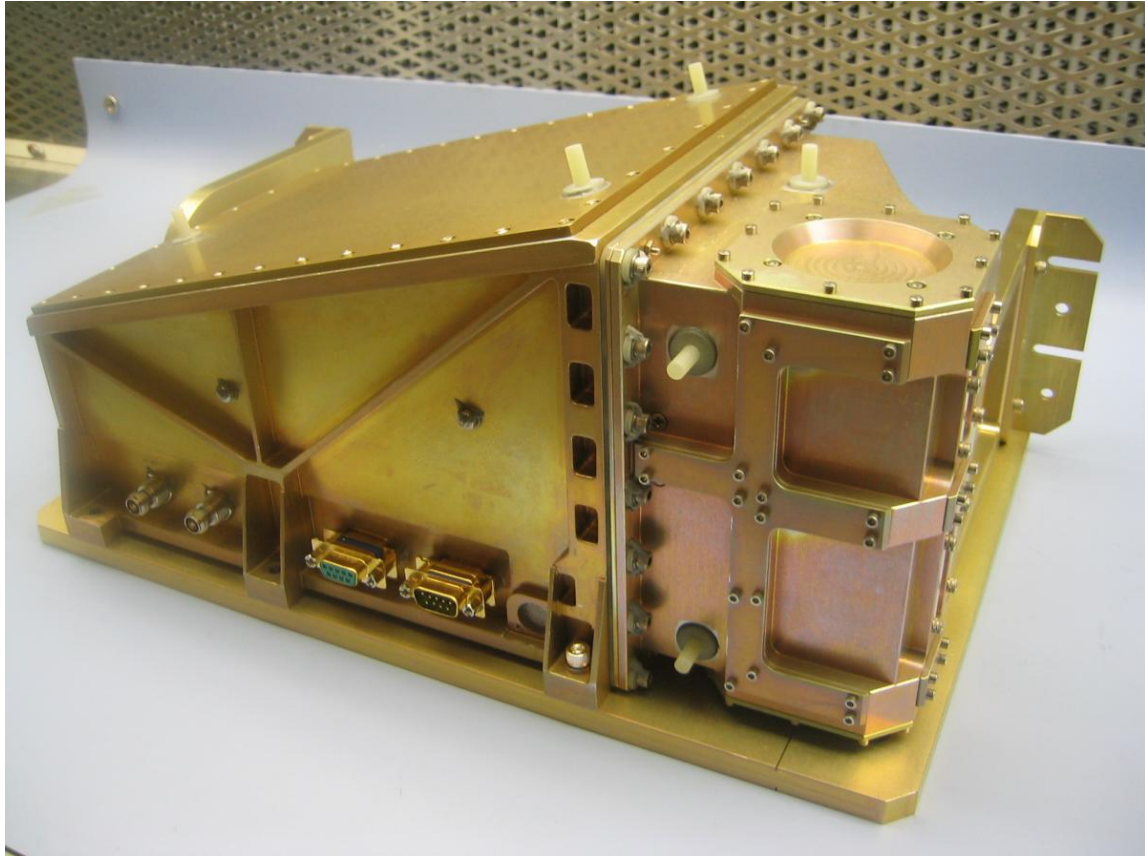
Figure 2. CRaTER flight model: telescope assembly is the rightmost portion while the signal processing section and spacecraft interface is in the slanted enclosure to the left.
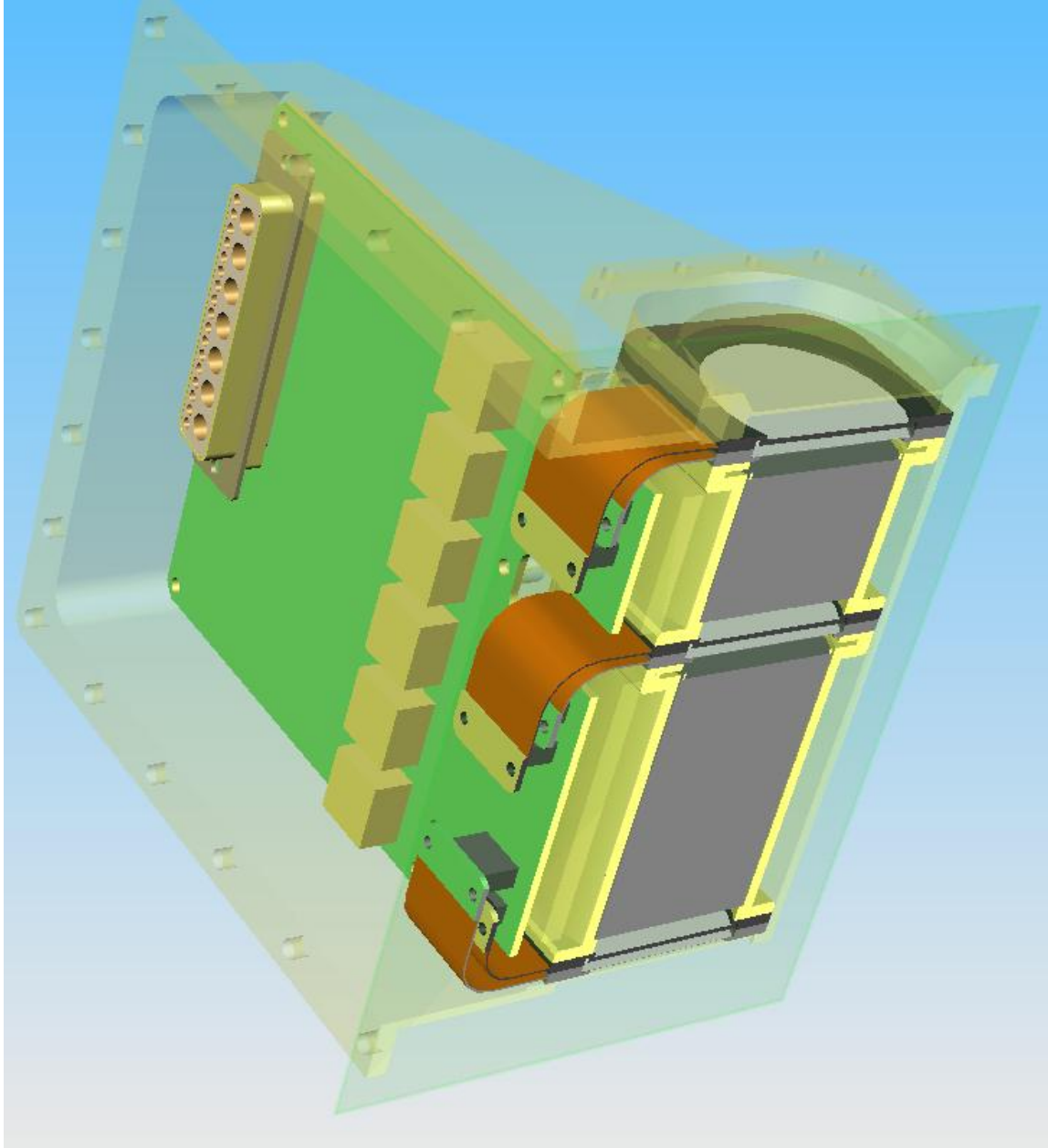
Figure 3. Cross-section schematic of the telescope assembly, showing the two sections of TEP (gray) sandwiched between three detector pairs, connected via flexible cables (brown) to the analog signal processing board (green).
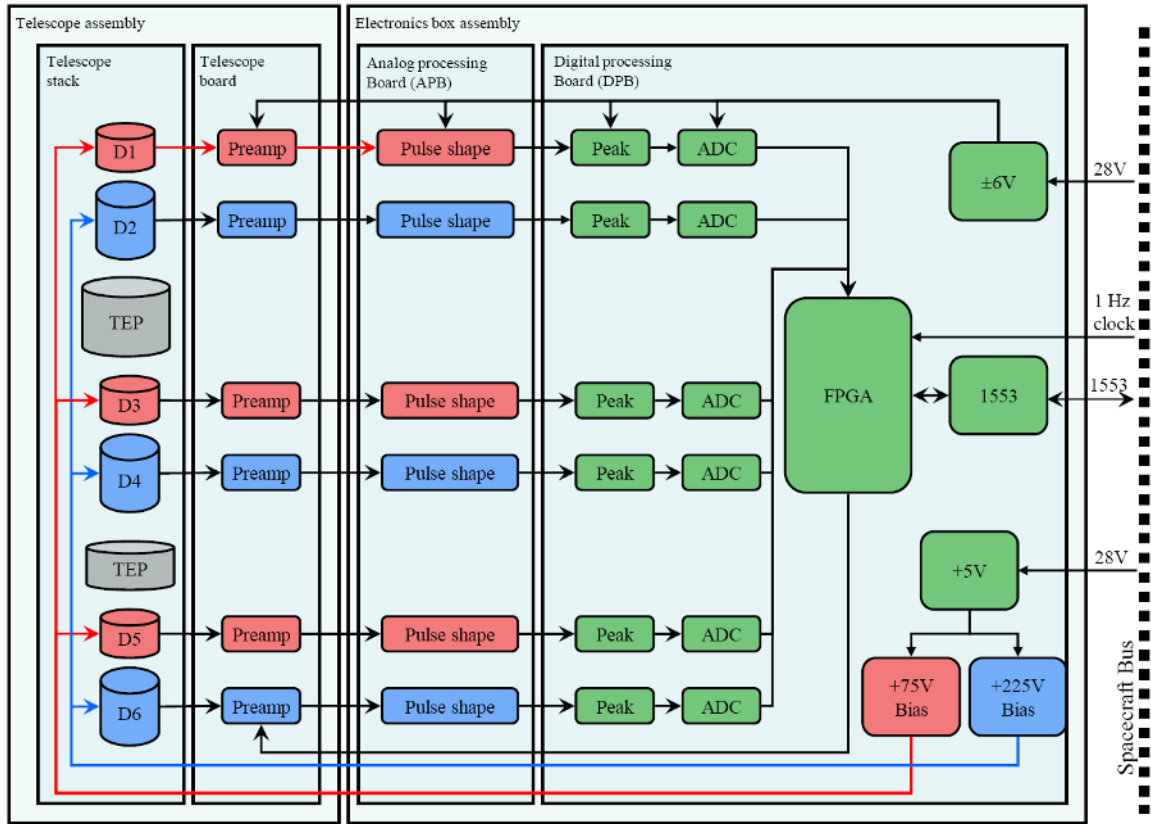
Figure 4. CRaTER functional block diagram showing the critical components of the instrument. Particle detection, signal processing, and communication with the LRO spacecraft flow from left to right.
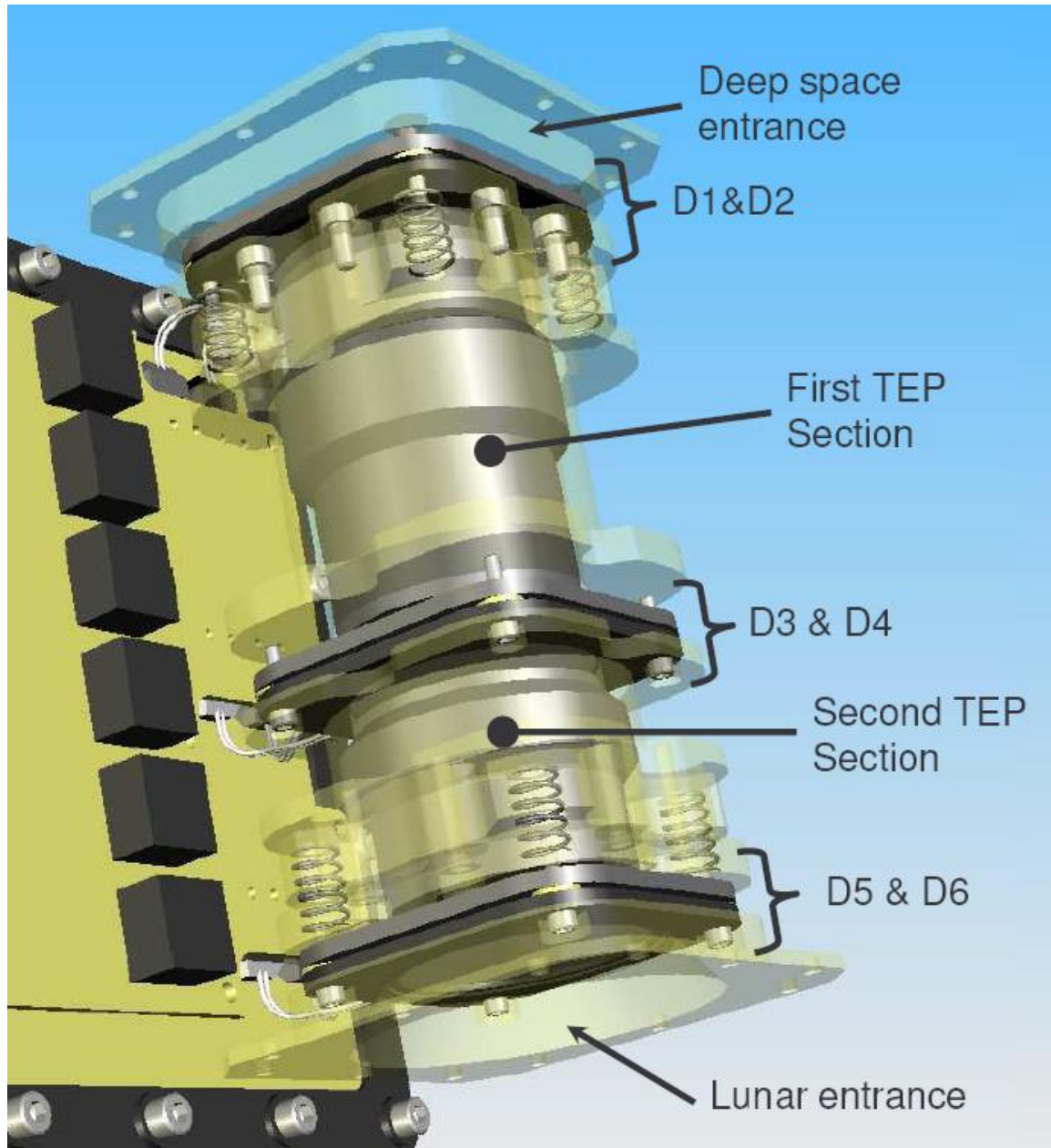
Figure 5. Transparent view of the telescope assembly, showing the pairs of thin and thick detector sandwiching the two TEP volumes in the telescope stack, and the associated telescope electronics board. A cable with signal and ground runs from each of the detectors to one of six preamplifiers on the telescope electronics board.
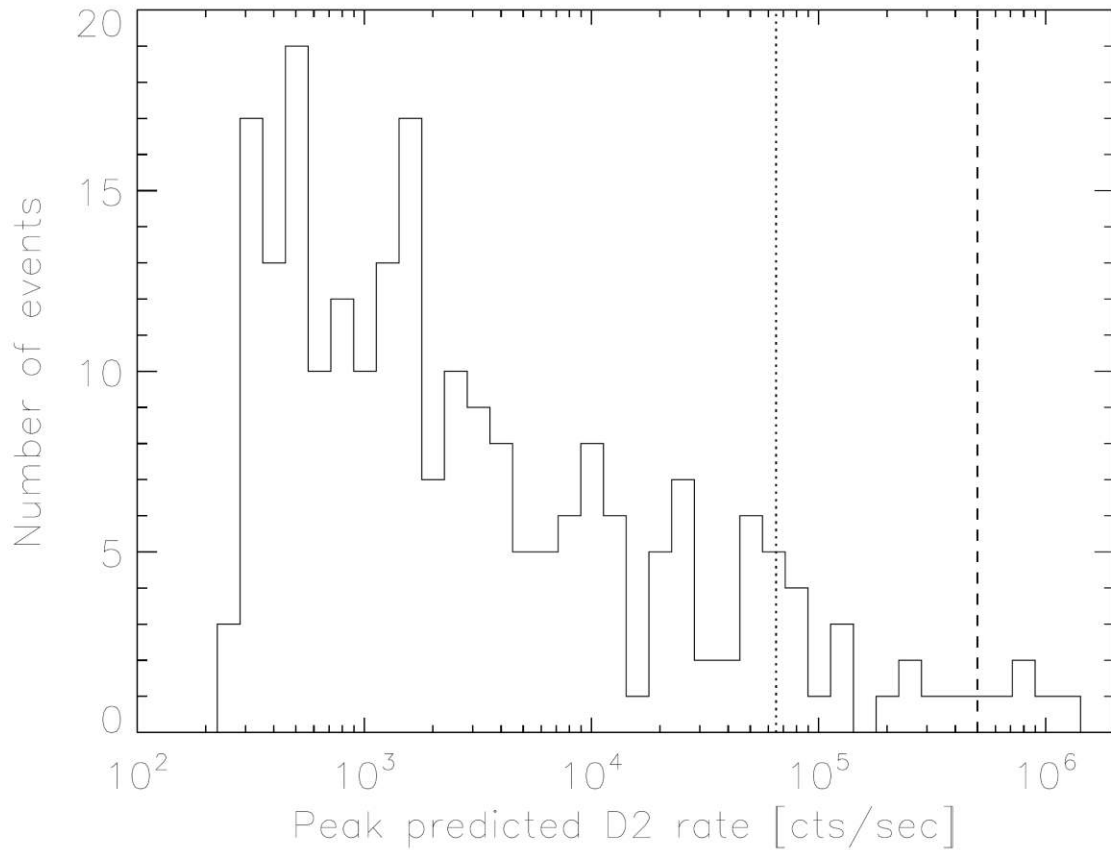
Figure 6. Predicted number of >10 MeV solar proton events versus 5-minute-average D2 peak rates, based on 33 years of GOES proton data. Approximately 90% of these 225 representative >10 MeV SEP events will be cleanly measured in CRaTER's normal operating mode; the 10% with rates higher than that delineated by the left-most vertical line will be measured cleanly in CRaTER's elevated rate model (see Section 3.3.6 for details). The vertical dotted line represents the instrumental limit for recording true rates; the vertical dashed line is the ideal analog electronic limit for event processing.
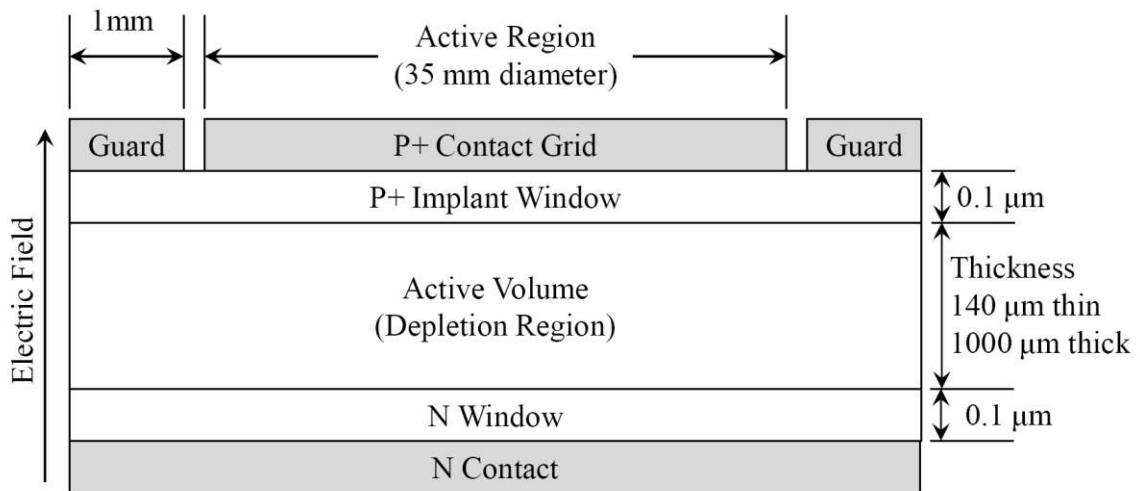
Figure 7. Schematic cross section of the silicon detectors in the CRaTER instrument.
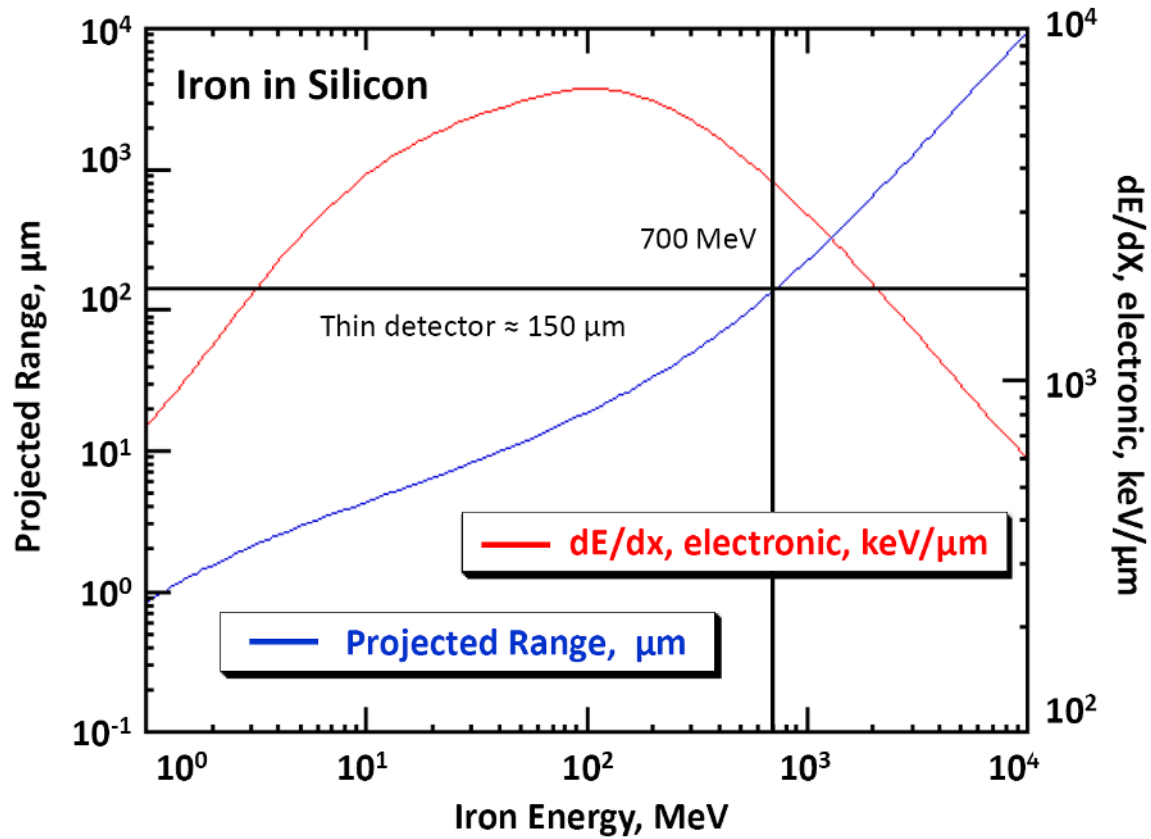
Figure 8. The upper energy range of the thin detectors is determined by the maximum energy expected from an iron nucleus as determined using SRIM (Ziegler et al., 1984). This is a plot of the projected range and LET of iron in silicon showing a peak energy of approximately 700 MeV.
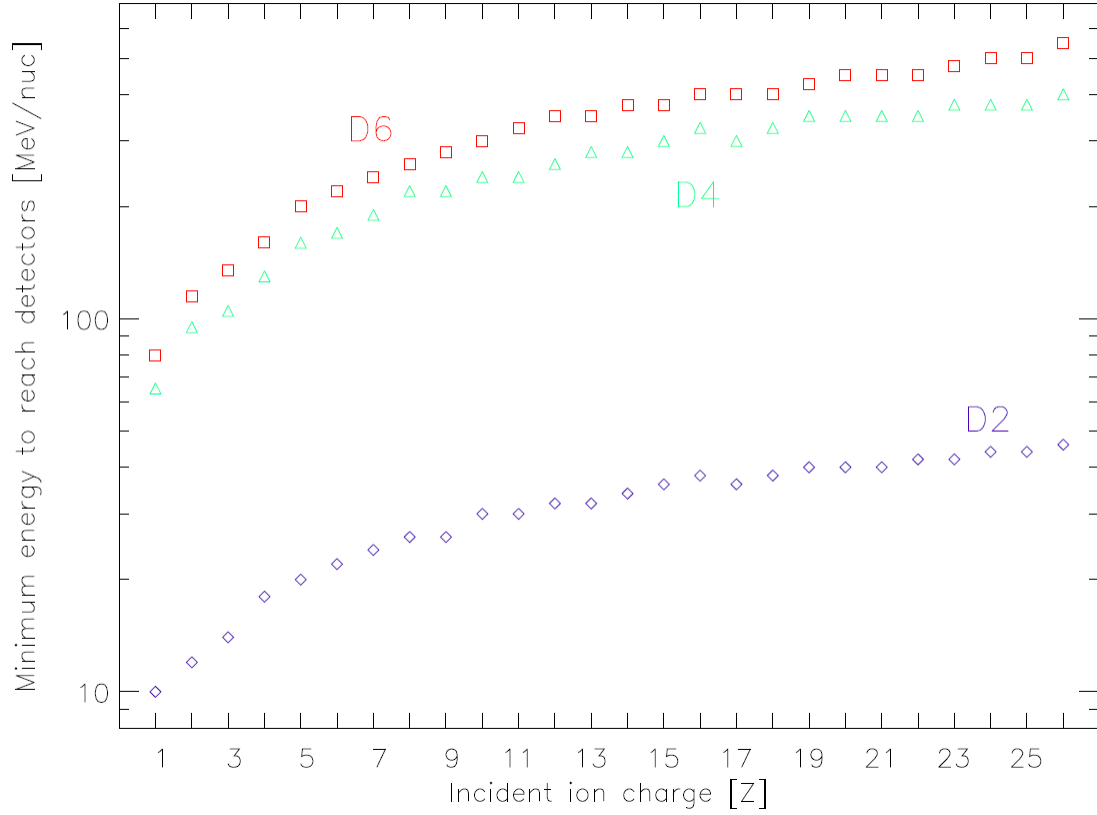
Figure 9. Minimum energy required of an incident ion, from hydrogen to iron (using each ion's most common isotope) normally-incident from the zenith direction to reach detectors D2 (lower blue curve), D4 (middle green curve), and D6 (upper red curve).
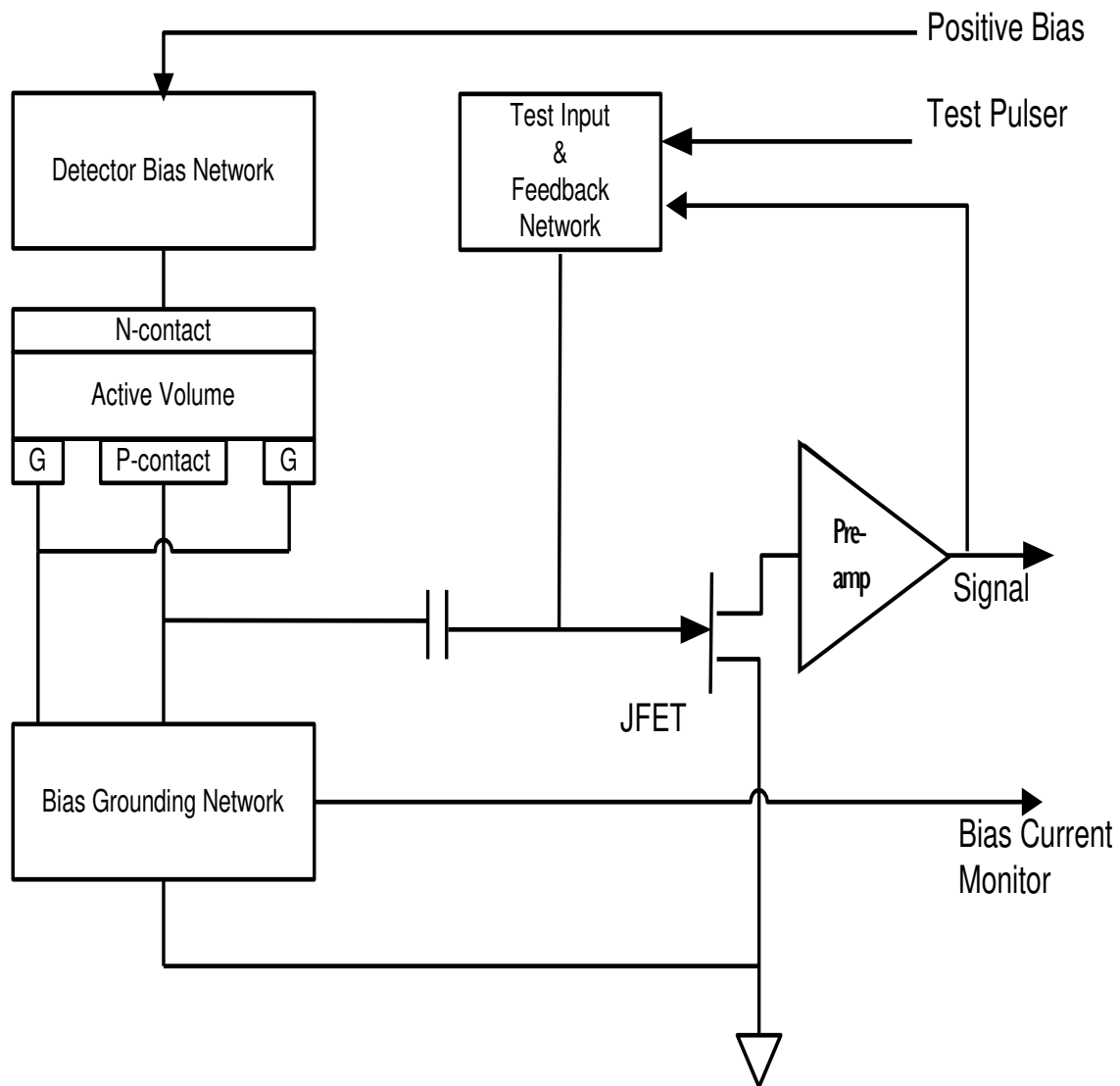
Figure 10. Schematic illustrating the components of the telescope board for a single detector. A positive voltage biases the detector on the N-contact with the signal coming off the P-contact. Bias grounding networks connect the P-contact and G-contact to ground. Current from the detector is AC coupled to a jFET and pre- amplifier and the amplified output signal is sent to the electronics box along with a bias current monitor. A feedback network dissipates the collected signal from the detector and accepts external test pulses from the electronics box for calibration purposes.
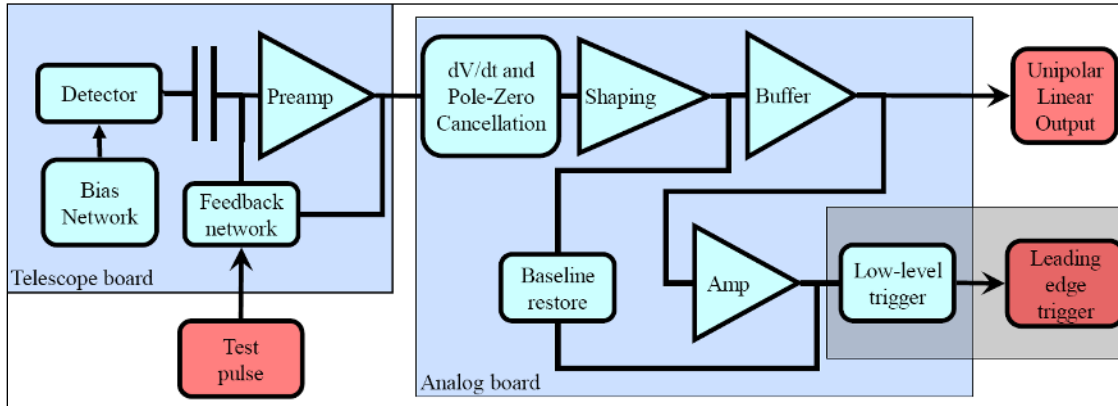
Figure 11. Block flow diagram illustrating the signal pulse shaping process. The preamp processes the signals from either the detector or the test pulser. The signal is then amplified and given an approximately 1 us pulse profile. A baseline restorer is used to help maintain the baseline voltage with larger events. The baseline restorer can also be used to generate a low level trigger - this feature is not used in the current design in flight but is used on the ground while testing the system.
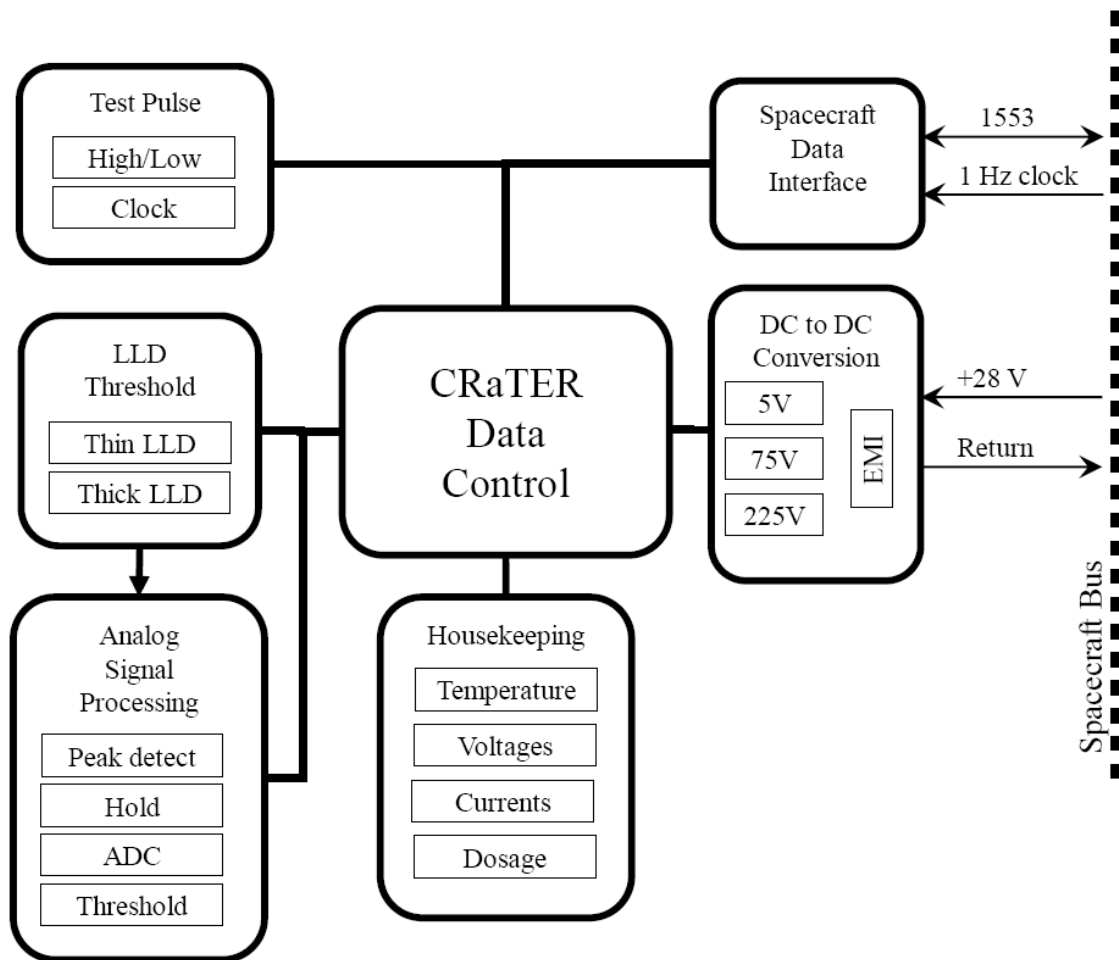
Figure 12. Block diagram of the digital system. The FPGA generates test pulses for calibration and broadcasts the LLD for the thin and thick detectors, performs the PHA, enables bias voltages, and monitors housekeeping data such as temperatures, voltages, currents, and total dose within the telescope. The FPGA communicates to the spacecraft through the 1553 interface and receives the 1 Hz clock from the spacecraft.
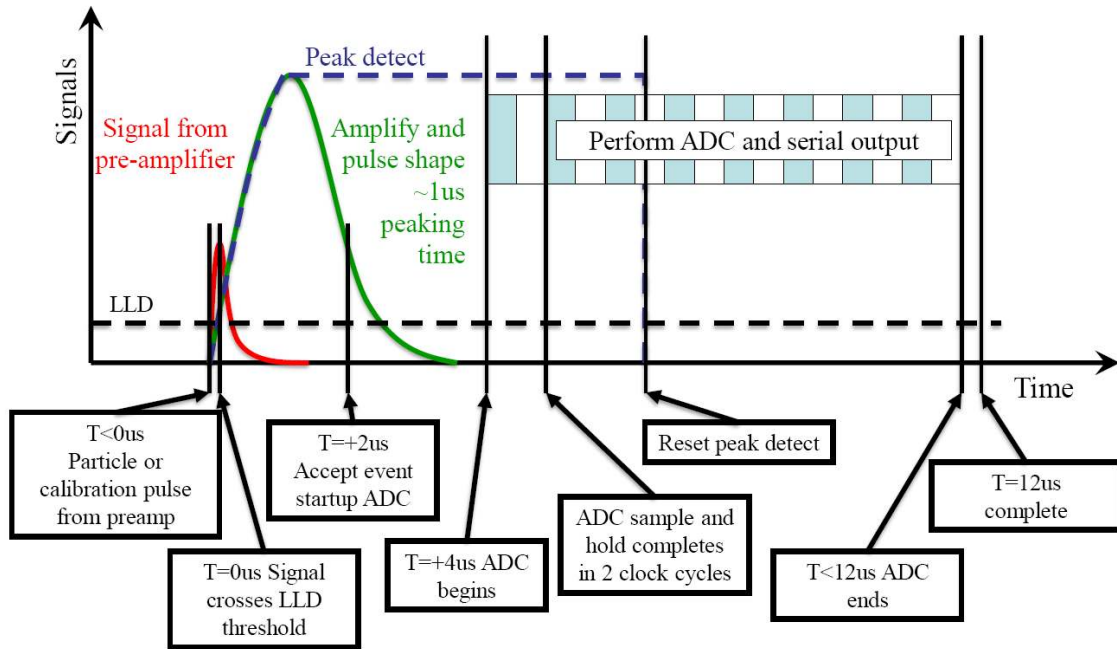
Figure 13. Schematic illustration of the pulse height analysis (PHA) process on the analog and digital boards in the electronics box.
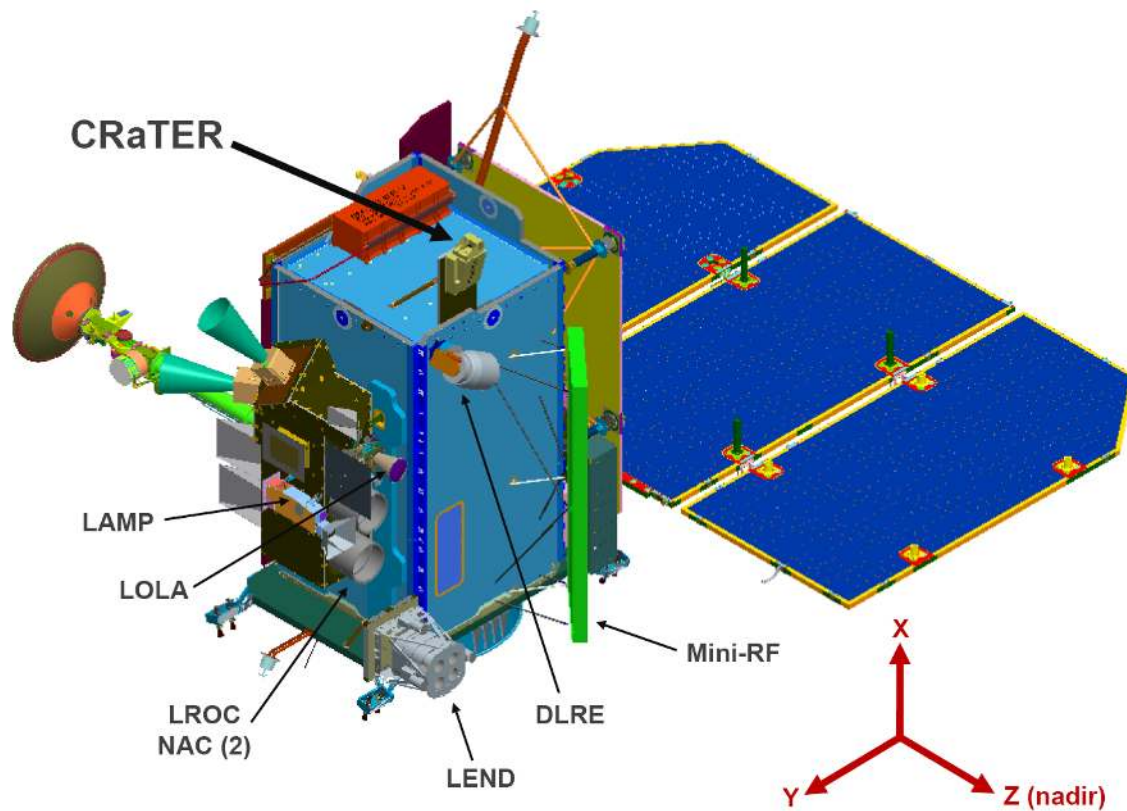
Figure 14. CRaTER mounting location on the LRO spacecraft. The positive z-axis points toward lunar nadir during normal flight operations; the positive x-axis points nominally along LRO's orbital velocity vector.
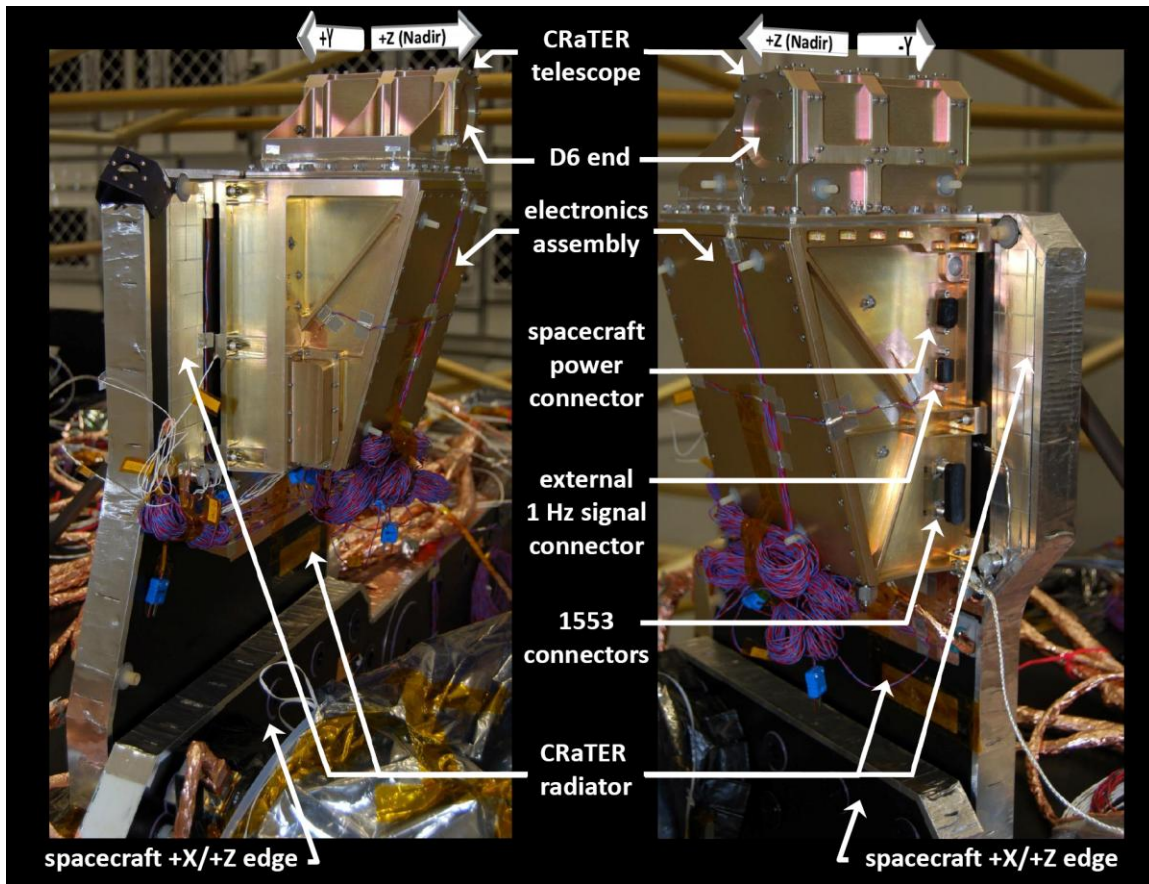
Figure 15. Two labeled views of the CRaTER flight unit as mounted to the LRO spacecraft during final integration and before thermal blanket attachment. The nadir direction (+z) is labeled in each view for perspective.
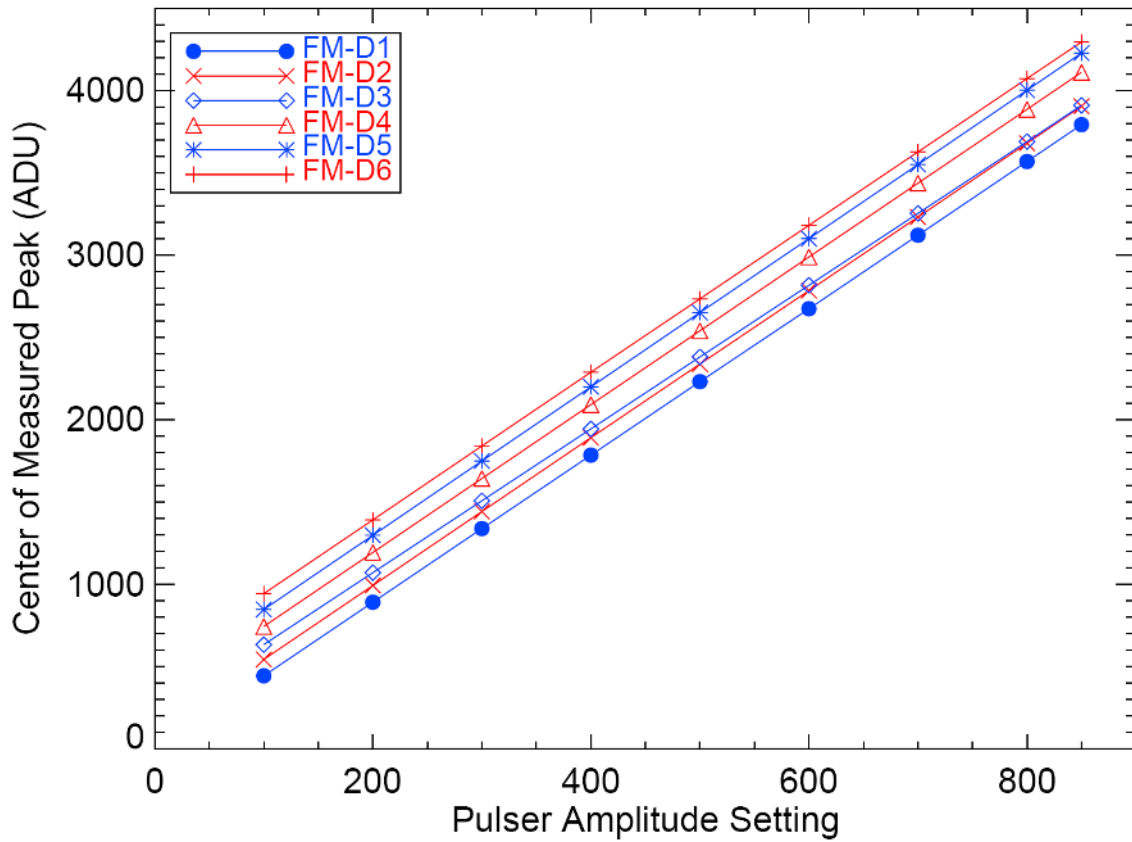
Figure 16. Demonstration of the linearity of the pulse height analysis circuitry for all detectors of the FM using the external pulse generator, performed at a typical in-flight temperature of 10° C. The center of the measured peak value is offset by 100 ADU successively between detectors (starting from D1) in order to better demonstrate linearity of each chain.
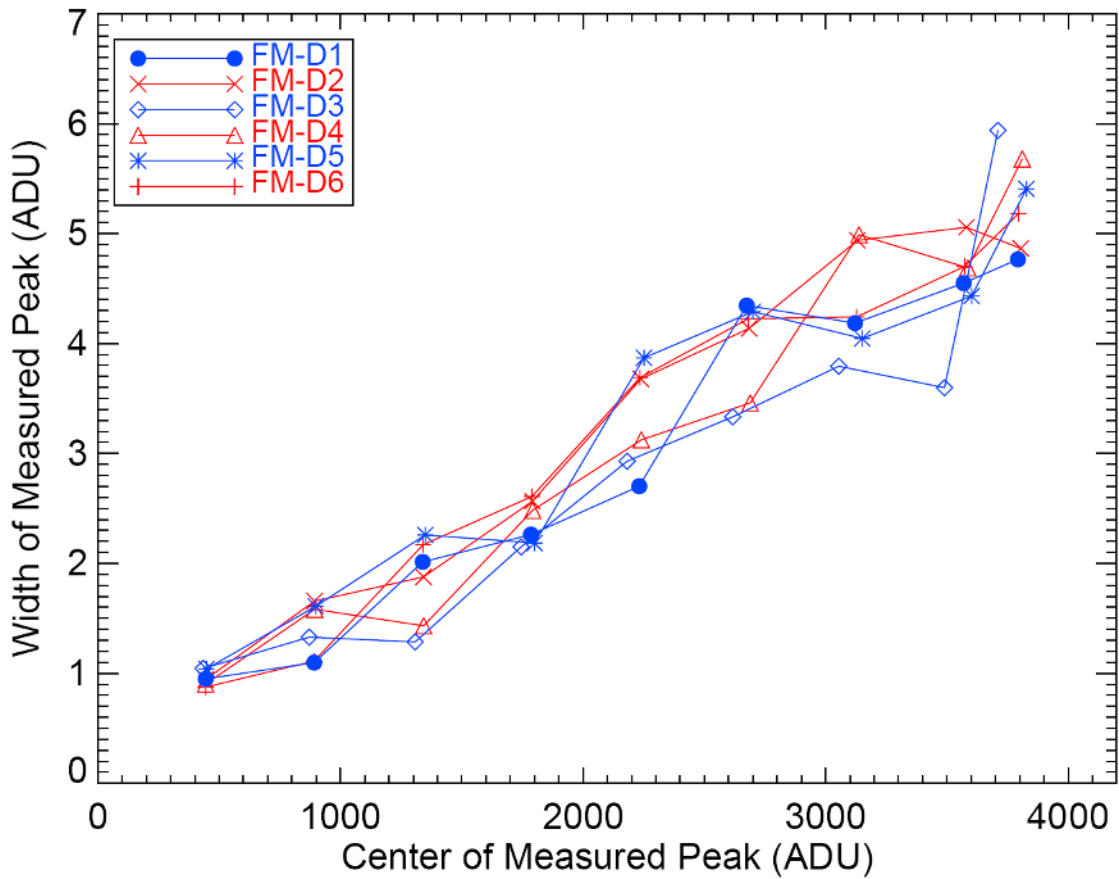
Figure 17. Standard deviation of measured PHA peak values (in ADU) returned as a function of the center of the measured peak (in ADU) for nine externally generated pulse amplitudes in all six detectors of the FM with the telescope operating at 10°C. This shows that the noise level of the electronics is a constant fraction of the input pulse amplitude, and is less than about 0.15%.
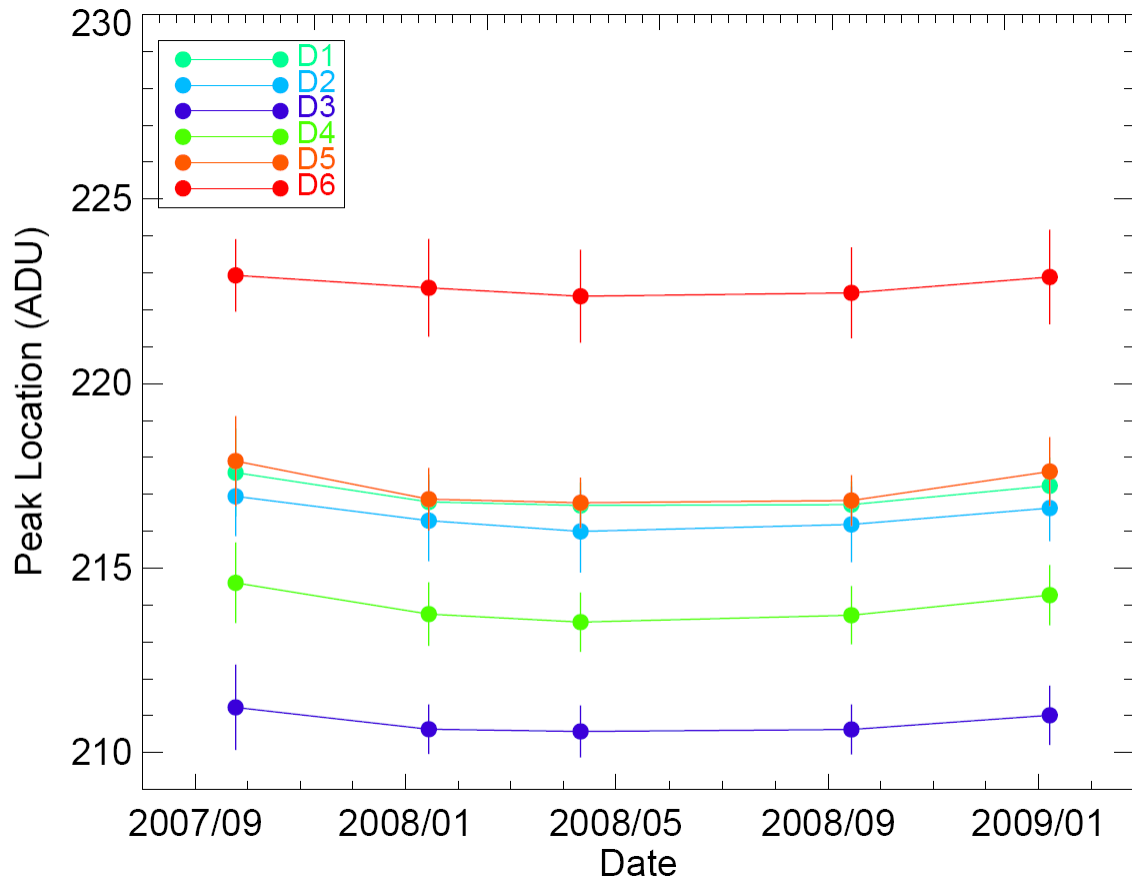
Figure 18. Measured center of signal peak (in ADU) in the FM generated by the internal pulse generator at a fixed setting, during five internal calibration runs spaced over nearly 18 months. The FM response remained steady and reproducible at the ~0.06% level.
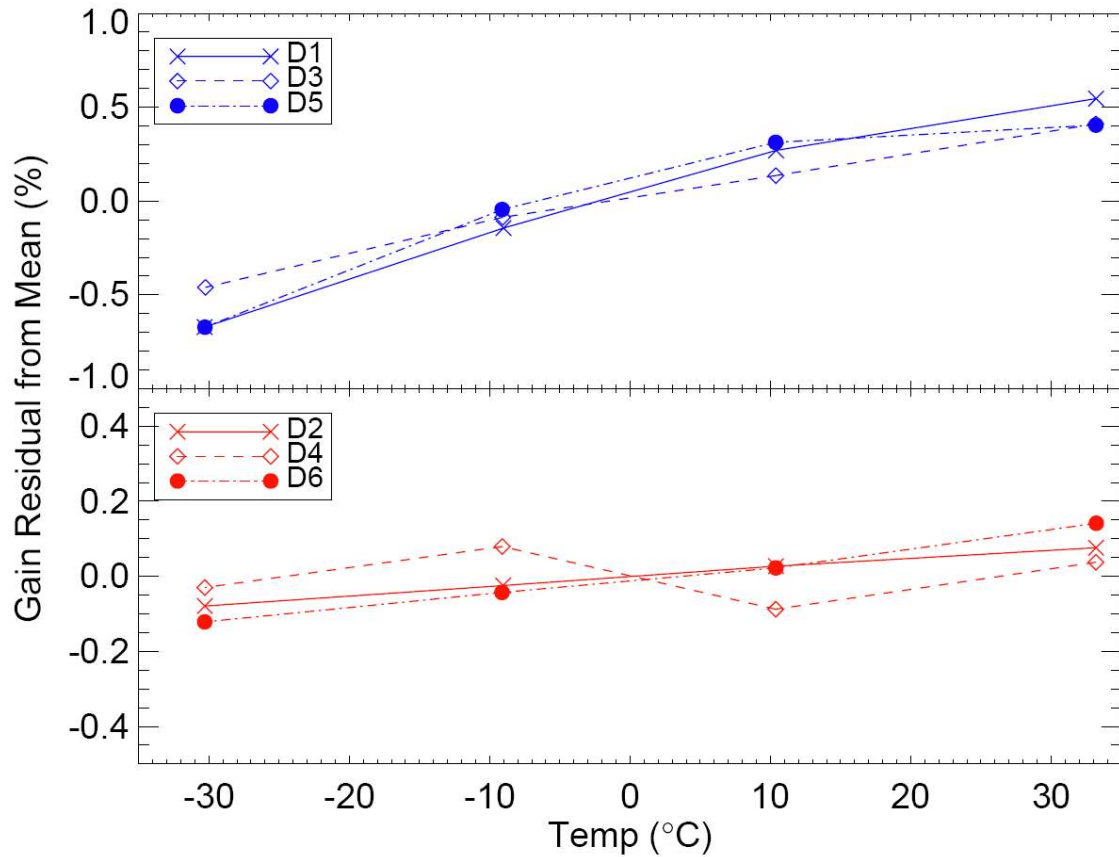
Figure 19. Response of measured gain of a fixed external pulse generator amplitude versus temperature, ranging from -30° to +35°C. Total percentage gain change across the full temperature range is only ±0.1% for the thick detectors (D2, D4, D6) and is only only ±0.5% for the thin detectors (D1, D3, D5).
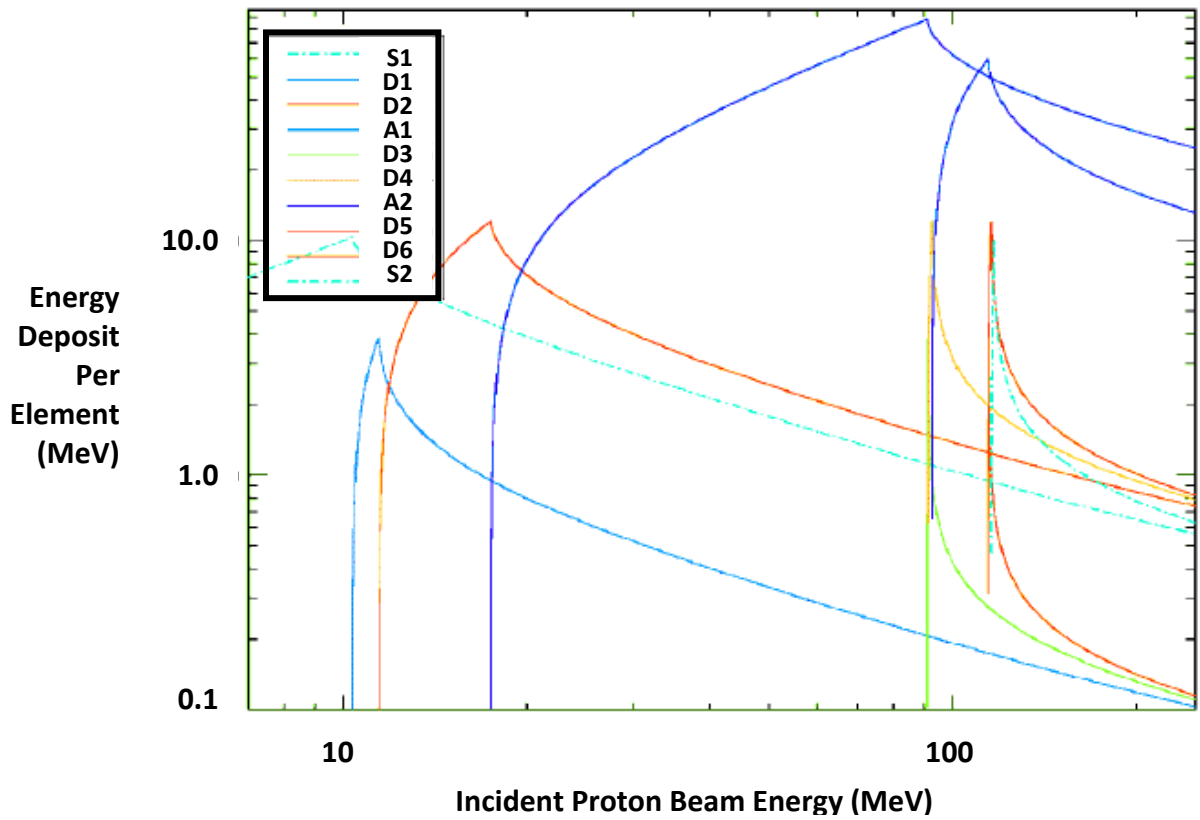
Figure 20. Calculations of energy loss in each component of the CRaTER telescope stack as a function of initial energy of incident protons using the SRIM program, showing the regions of peak energy response for each detector in the telescope.
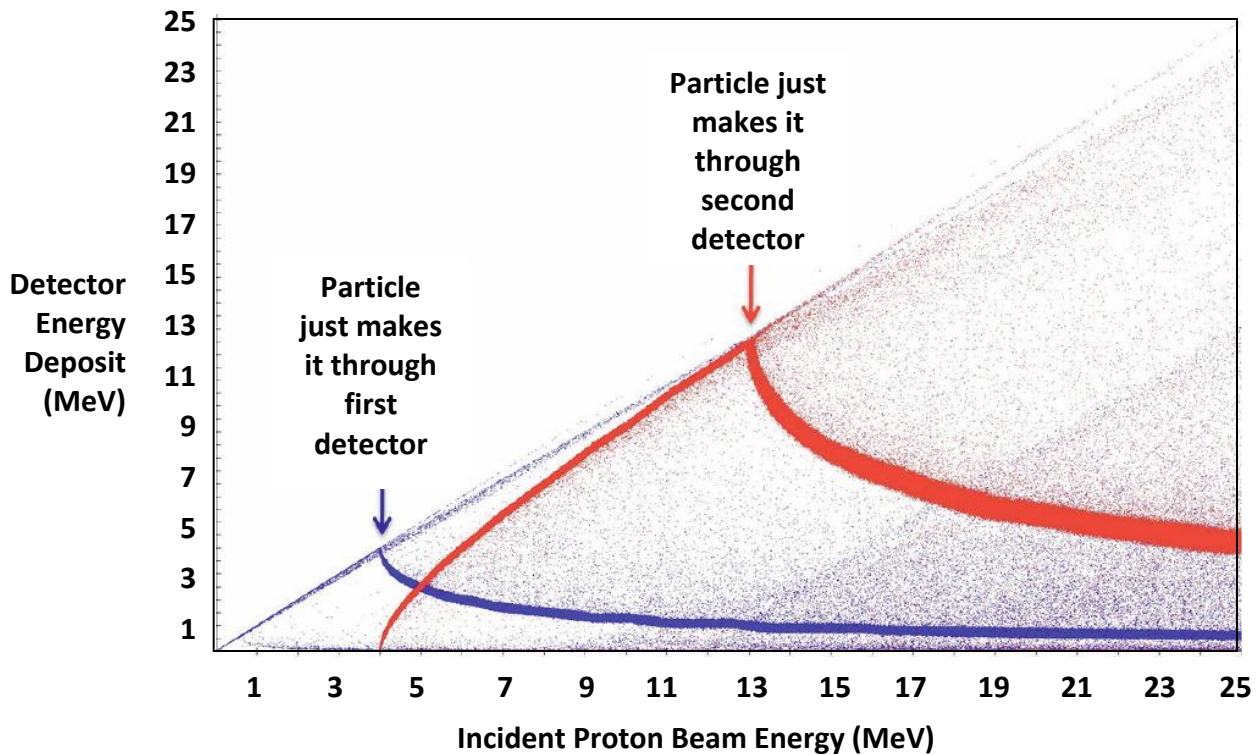
Figure 21. A scatter plot of the energy deposited in a pair of thin and thick detectors as a function of incident energy. Unlike the previous two calculations shown in this section, this simulation makes use of the Geant4 code, which includes more accurate physics including scattering and nuclear interactions.
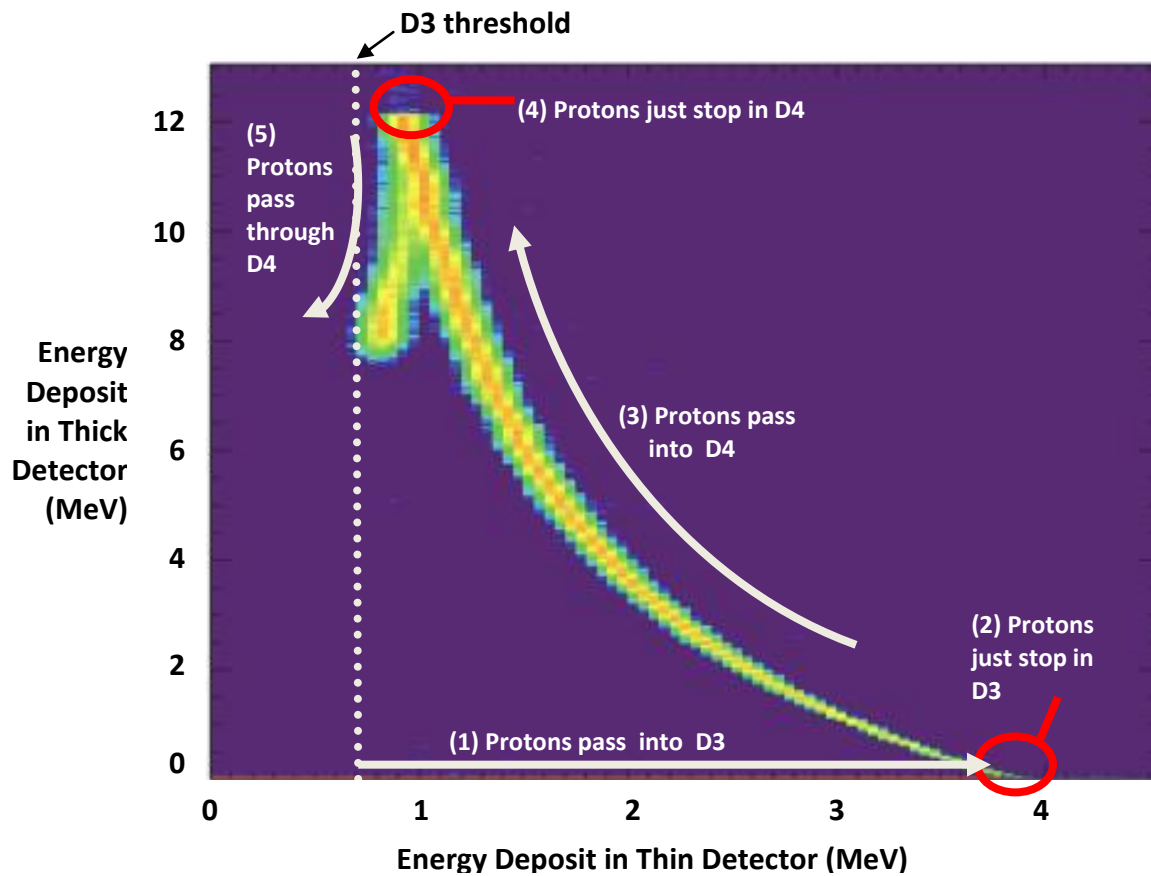
Figure 22. Two-dimensional histogram of simulated protons depositing energy in D3 (horizontal axis), a thin detector, and D4 (vertical axis), a thick detector. The arrows illustrate the track that proton energy deposition follows in the histogram as a function of increasing initial proton energy. The encircled red locations are the unique locations in energy space where protons are just stopping in either D3 (location #2) or D4 (location #4).
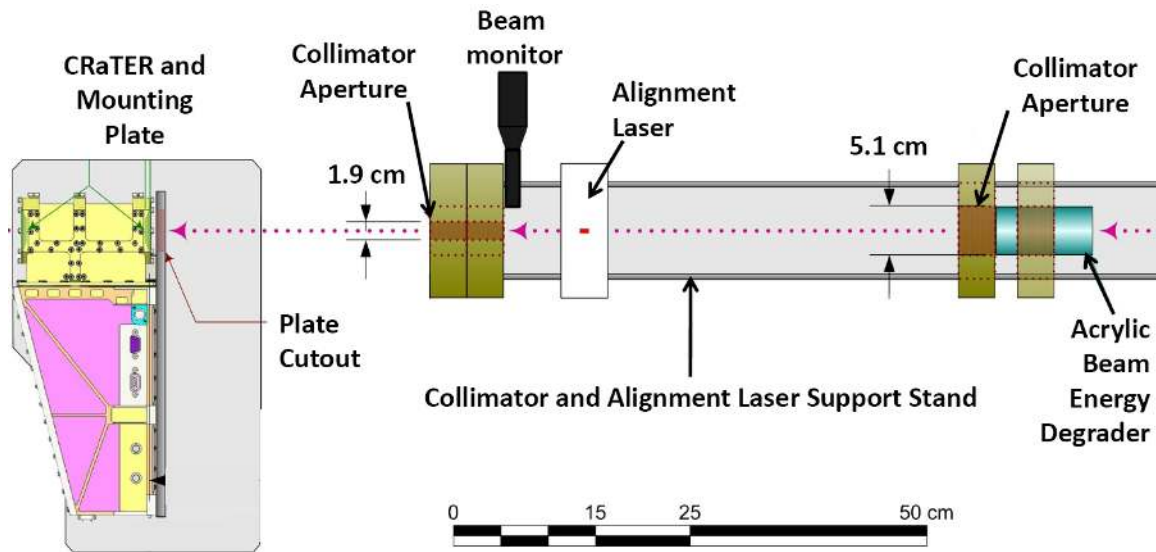
Figure 23. Beam line geometry and configuration for typical testing of CRaTER EM and FM units at the MGH proton facility.
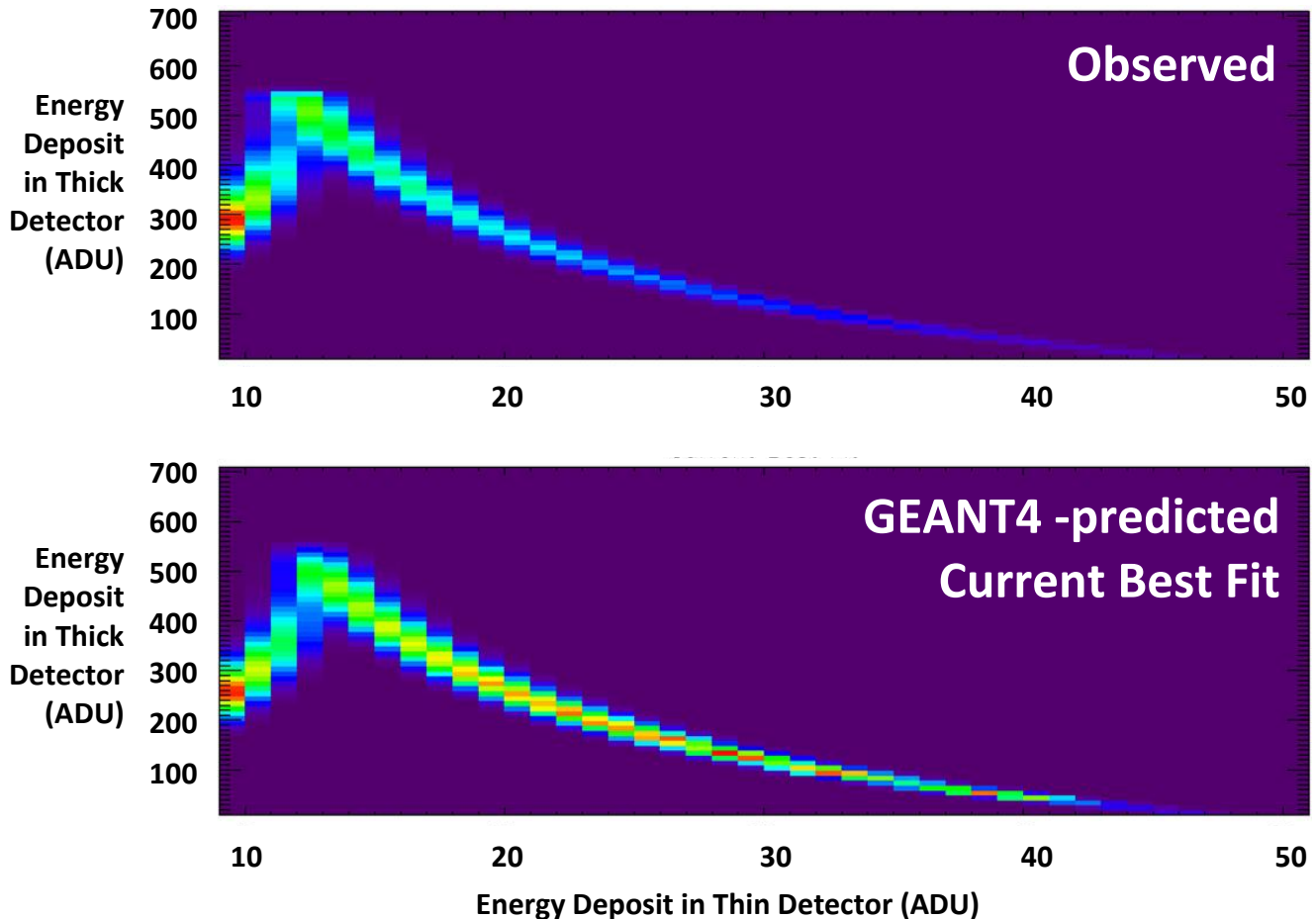
Figure 24.   The top panel displays a histogram of energy deposits (expressed in ADU) in D3 (horizontal axis) and D4 (vertical axis) obtained when the CRaTER FM was being irradiated with protons. Color coding indicates relative number of energy deposits at each point in the two-dimensional histogram (purple is the zero level, ranging to red at the highest level). The bottom panel displays a comparable histogram as predicted by the GEANT4 model, demonstrating one iterative step in the end-to-end calibration process.

Figure 25.   The basic architecture of the CRaTER Science Operations Center.

Raw
- Raw science and housekeeping data files (*.sci, *.hk)
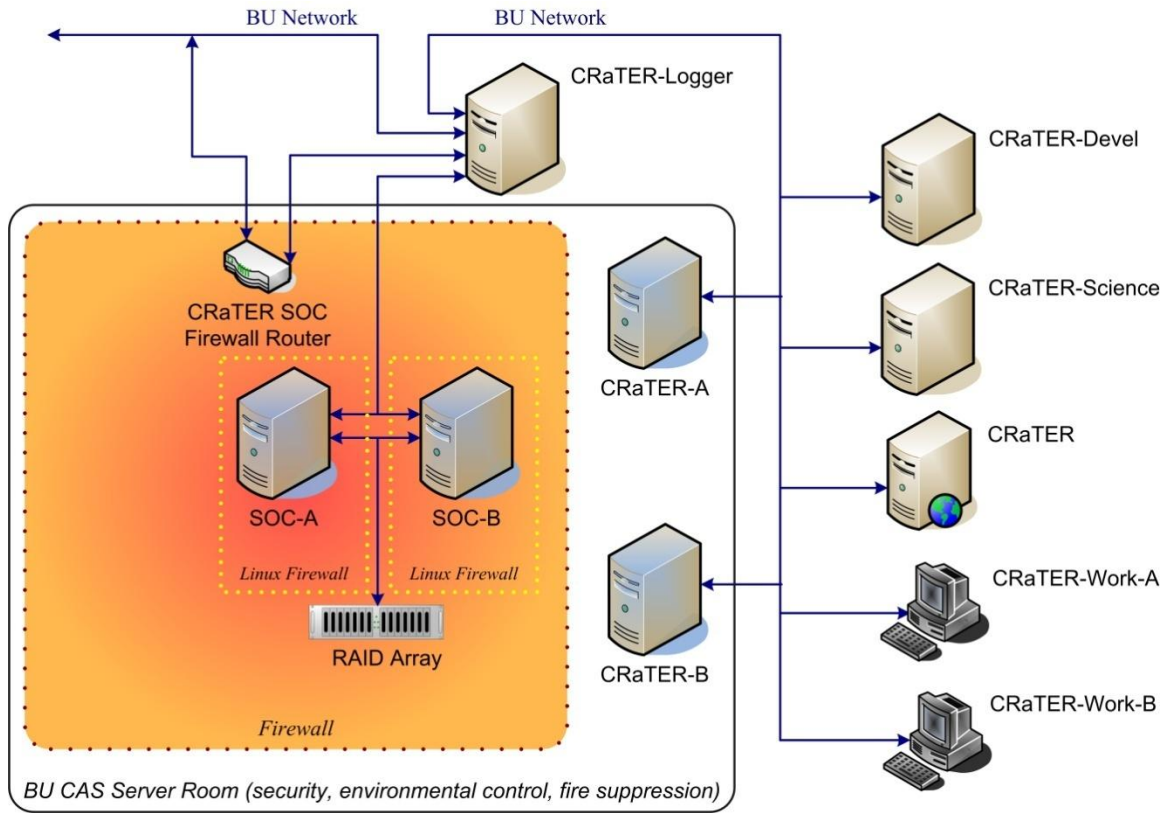- MOC and FDF data products

L0
- Data within specified GMT day (00:00:00 to 23:59:59 UTC)
- Time ordered data
- Duplicate, mismatched, and corrupted data packets removed
- Separate files for primary science, secondary science, and instrument housekeeping
- Files in binary format

L1
- Primary science data converted to energy deposit per detector
- Secondary science data unchanged from L0
- Housekeeping data converted to engineering units
- Separate files for primary science, secondary science, and instrument housekeeping
- Files in ASCII format

L2
- Primary science data converted to LET in each detector
- Spacecraft location and orientation added to L1 secondary science data
- Separate files for primary science, secondary science, and instrument housekeeping
- Files in ASCII format

Archive
- L0, L1, and L2 data files + PDS detached label files
- Quick-look plots + PDS detached label files
- Data gap and mode change logs
- MOC and FDF data products, raw science measurement and housekeeping summaries
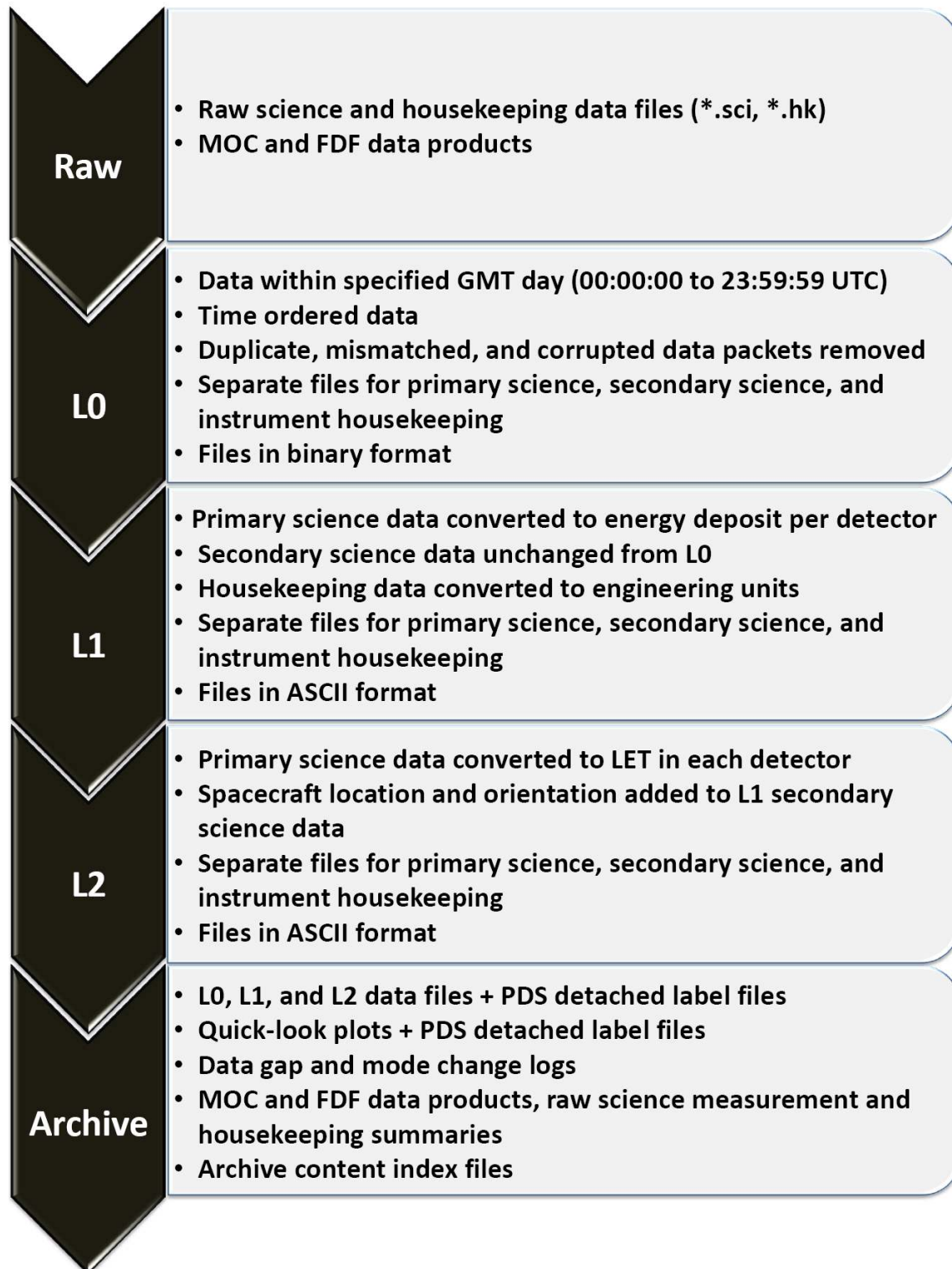- Archive content index files

Figure 26.   The pipeline processing flow diagram outlining up to the Level 2 CRaTER data delivered to the Planetary Data System archive.